EUROPEAN LABORATORY FOR PARTICLE PHYSICS

CERN-EP/98-136
18th August 1998

Search for Chargino and Neutralino Production at $\sqrt{s} = 181$–184 GeV at LEP

The OPAL Collaboration

Abstract

A search for charginos and neutralinos, predicted by supersymmetric theories, has been performed using a data sample of 57 pb^{-1} at centre-of-mass energies of 181–184 GeV taken with the OPAL detector at LEP. No evidence for chargino or neutralino production has been found. Upper limits on chargino and neutralino pair production ($\tilde{\chi}_1^+\tilde{\chi}_1^-$,$\tilde{\chi}_1^0\tilde{\chi}_2^0$) cross-sections are obtained as a function of the chargino mass ($m_{\tilde{\chi}_1^\pm}$), the lightest neutralino mass ($m_{\tilde{\chi}_1^0}$) and the second lightest neutralino mass ($m_{\tilde{\chi}_2^0}$). For large chargino masses the limits have been improved with respect to the previous analyses at lower centre-of-mass energies. Exclusion regions at 95% confidence level (C.L.) of parameters of the Constrained Minimal Supersymmetric Standard Model are determined for the case of a large universal scalar mass, m_0, implying heavy scalar fermions, and for the case of a small m_0 resulting in light scalar fermions and giving the worst-case limits. Within this framework and for $m_{\tilde{\chi}_1^\pm} - m_{\tilde{\chi}_1^0} \geq 5$ GeV the 95% C.L. lower limits on $m_{\tilde{\chi}_1^\pm}$ for $m_0 =$ 500 GeV are 90.0 and 90.2 GeV for $\tan\beta = 1.5$ and 35 respectively. These limits for all m_0 (the worst-case) are 69.1 and 65.2 GeV for $\tan\beta = 1.5$ and 35 respectively. Exclusion regions are also presented for neutralino masses, including an absolute lower limit at 95% C.L. for the mass of the lightest neutralino of 30.1 GeV for $m_0 = 500$ GeV (24.2 GeV for all m_0), with implications for experimental searches for the lightest neutralino as a dark matter candidate.

Submitted to Eur. Phys. Journal C

G. Abbiendi[2], K. Ackerstaff[8], G. Alexander[23], J. Allison[16], N. Altekamp[5], K.J. Anderson[9], S. Anderson[12], S. Arcelli[17], S. Asai[24], S.F. Ashby[1], D. Axen[29], G. Azuelos[18,a], A.H. Ball[17], E. Barberio[8], R.J. Barlow[16], R. Bartoldus[3], J.R. Batley[5], S. Baumann[3], J. Bechtluft[14], T. Behnke[27], K.W. Bell[20], G. Bella[23], A. Bellerive[9], S. Bentvelsen[8], S. Bethke[14], S. Betts[15], O. Biebel[14], A. Biguzzi[5], S.D. Bird[16], V. Blobel[27], I.J. Bloodworth[1], M. Bobinski[10], P. Bock[11], J. Böhme[14], D. Bonacorsi[2], M. Boutemeur[34], S. Braibant[8], P. Bright-Thomas[1], L. Brigliadori[2], R.M. Brown[20], H.J. Burckhart[8], C. Burgard[8], R. Bürgin[10], P. Capiluppi[2], R.K. Carnegie[6], A.A. Carter[13], J.R. Carter[5], C.Y. Chang[17], D.G. Charlton[1,b], D. Chrisman[4], C. Ciocca[2], P.E.L. Clarke[15], E. Clay[15], I. Cohen[23], J.E. Conboy[15], O.C. Cooke[8], C. Couyoumtzelis[13], R.L. Coxe[9], M. Cuffiani[2], S. Dado[22], G.M. Dallavalle[2], R. Davis[30], S. De Jong[12], L.A. del Pozo[4], A. de Roeck[8], K. Desch[8], B. Dienes[33,d], M.S. Dixit[7], J. Dubbert[34], E. Duchovni[26], G. Duckeck[34], I.P. Duerdoth[16], D. Eatough[16], P.G. Estabrooks[6], E. Etzion[23], H.G. Evans[9], F. Fabbri[2], M. Fanti[2], A.A. Faust[30], F. Fiedler[27], M. Fierro[2], I. Fleck[8], R. Folman[26], A. Fürtjes[8], D.I. Futyan[16], P. Gagnon[7], J.W. Gary[4], J. Gascon[18], S.M. Gascon-Shotkin[17], G. Gaycken[27], C. Geich-Gimbel[3], G. Giacomelli[2], P. Giacomelli[2], V. Gibson[5], W.R. Gibson[13], D.M. Gingrich[30,a], D. Glenzinski[9], J. Goldberg[22], W. Gorn[4], C. Grandi[2], E. Gross[26], J. Grunhaus[23], M. Gruwé[27], G.G. Hanson[12], M. Hansroul[8], M. Hapke[13], K. Harder[27], C.K. Hargrove[7], C. Hartmann[3], M. Hauschild[8], C.M. Hawkes[5], R. Hawkings[27], R.J. Hemingway[6], M. Herndon[17], G. Herten[10], R.D. Heuer[8], M.D. Hildreth[8], J.C. Hill[5], S.J. Hillier[1], P.R. Hobson[25], A. Hocker[9], R.J. Homer[1], A.K. Honma[28,a], D. Horváth[32,c], K.R. Hossain[30], R. Howard[29], P. Hüntemeyer[27], P. Igo-Kemenes[11], D.C. Imrie[25], K. Ishii[24], F.R. Jacob[20], A. Jawahery[17], H. Jeremie[18], M. Jimack[1], C.R. Jones[5], P. Jovanovic[1], T.R. Junk[6], D. Karlen[6], V. Kartvelishvili[16], K. Kawagoe[24], T. Kawamoto[24], P.I. Kayal[30], R.K. Keeler[28], R.G. Kellogg[17], B.W. Kennedy[20], A. Klier[26], S. Kluth[8], T. Kobayashi[24], M. Kobel[3,e], D.S. Koetke[6], T.P. Kokott[3], M. Kolrep[10], S. Komamiya[24], R.V. Kowalewski[28], T. Kress[11], P. Krieger[6], J. von Krogh[11], T. Kuhl[3], P. Kyberd[13], G.D. Lafferty[16], D. Lanske[14], J. Lauber[15], S.R. Lautenschlager[31], I. Lawson[28], J.G. Layter[4], D. Lazic[22], A.M. Lee[31], D. Lellouch[26], J. Letts[12], L. Levinson[26], R. Liebisch[11], B. List[8], C. Littlewood[5], A.W. Lloyd[1], S.L. Lloyd[13], F.K. Loebinger[16], G.D. Long[28], M.J. Losty[7], J. Ludwig[10], D. Liu[12], A. Macchiolo[2], A. Macpherson[30], W. Mader[3], M. Mannelli[8], S. Marcellini[2], C. Markopoulos[13], A.J. Martin[13], J.P. Martin[18], G. Martinez[17], T. Mashimo[24], P. Mättig[26], W.J. McDonald[30], J. McKenna[29], E.A. Mckigney[15], T.J. McMahon[1], R.A. McPherson[28], F. Meijers[8], S. Menke[3], F.S. Merritt[9], H. Mes[7], J. Meyer[27], A. Michelini[2], S. Mihara[24], G. Mikenberg[26], D.J. Miller[15], R. Mir[26], W. Mohr[10], A. Montanari[2], T. Mori[24], K. Nagai[8], I. Nakamura[24], H.A. Neal[12], B. Nellen[3], R. Nisius[8], S.W. O'Neale[1], F.G. Oakham[7], F. Odorici[2], H.O. Ogren[12], M.J. Oreglia[9], S. Orito[24], J. Pálinkás[33,d], G. Pásztor[32], J.R. Pater[16], G.N. Patrick[20], J. Patt[10], R. Perez-Ochoa[8], S. Petzold[27], P. Pfeifenschneider[14], J.E. Pilcher[9], J. Pinfold[30], D.E. Plane[8], P. Poffenberger[28], J. Polok[8], M. Przybycień[8], C. Rembser[8], H. Rick[8], S. Robertson[28], S.A. Robins[22], N. Rodning[30], J.M. Roney[28], K. Roscoe[16], A.M. Rossi[2], Y. Rozen[22], K. Runge[10], O. Runolfsson[8], D.R. Rust[12], K. Sachs[10], T. Saeki[24], O. Sahr[34], W.M. Sang[25], E.K.G. Sarkisyan[23], C. Sbarra[29], A.D. Schaile[34], O. Schaile[34], F. Scharf[3], P. Scharff-Hansen[8], J. Schieck[11], B. Schmitt[8], S. Schmitt[11], A. Schöning[8], M. Schröder[8], M. Schumacher[3], C. Schwick[8], W.G. Scott[20], R. Seuster[14], T.G. Shears[8], B.C. Shen[4], C.H. Shepherd-Themistocleous[8], P. Sherwood[15], G.P. Siroli[2], A. Sittler[27], A. Skuja[17], A.M. Smith[8], G.A. Snow[17], R. Sobie[28], S. Söldner-Rembold[10], M. Sproston[20], A. Stahl[3], K. Stephens[16], J. Steuerer[27], K. Stoll[10], D. Strom[19], R. Ströhmer[34], B. Surrow[8], S.D. Talbot[1], S. Tanaka[24], P. Taras[18], S. Tarem[22], R. Teuscher[8], M. Thiergen[10], M.A. Thomson[8], E. von Törne[3], E. Torrence[8], S. Towers[6], I. Trigger[18], Z. Trócsányi[33],

E. Tsur[23], A.S. Turcot[9], M.F. Turner-Watson[8], R. Van Kooten[12], P. Vannerem[10], M. Verzocchi[10], H. Voss[3], F. Wäckerle[10], A. Wagner[27], C.P. Ward[5], D.R. Ward[5], P.M. Watkins[1], A.T. Watson[1], N.K. Watson[1], P.S. Wells[8], N. Wermes[3], J.S. White[6], G.W. Wilson[16], J.A. Wilson[1], T.R. Wyatt[16], S. Yamashita[24], G. Yekutieli[26], V. Zacek[18], D. Zer-Zion[8]

[1]School of Physics and Astronomy, University of Birmingham, Birmingham B15 2TT, UK
[2]Dipartimento di Fisica dell' Università di Bologna and INFN, I-40126 Bologna, Italy
[3]Physikalisches Institut, Universität Bonn, D-53115 Bonn, Germany
[4]Department of Physics, University of California, Riverside CA 92521, USA
[5]Cavendish Laboratory, Cambridge CB3 0HE, UK
[6]Ottawa-Carleton Institute for Physics, Department of Physics, Carleton University, Ottawa, Ontario K1S 5B6, Canada
[7]Centre for Research in Particle Physics, Carleton University, Ottawa, Ontario K1S 5B6, Canada
[8]CERN, European Organisation for Particle Physics, CH-1211 Geneva 23, Switzerland
[9]Enrico Fermi Institute and Department of Physics, University of Chicago, Chicago IL 60637, USA
[10]Fakultät für Physik, Albert Ludwigs Universität, D-79104 Freiburg, Germany
[11]Physikalisches Institut, Universität Heidelberg, D-69120 Heidelberg, Germany
[12]Indiana University, Department of Physics, Swain Hall West 117, Bloomington IN 47405, USA
[13]Queen Mary and Westfield College, University of London, London E1 4NS, UK
[14]Technische Hochschule Aachen, III Physikalisches Institut, Sommerfeldstrasse 26-28, D-52056 Aachen, Germany
[15]University College London, London WC1E 6BT, UK
[16]Department of Physics, Schuster Laboratory, The University, Manchester M13 9PL, UK
[17]Department of Physics, University of Maryland, College Park, MD 20742, USA
[18]Laboratoire de Physique Nucléaire, Université de Montréal, Montréal, Quebec H3C 3J7, Canada
[19]University of Oregon, Department of Physics, Eugene OR 97403, USA
[20]CLRC Rutherford Appleton Laboratory, Chilton, Didcot, Oxfordshire OX11 0QX, UK
[22]Department of Physics, Technion-Israel Institute of Technology, Haifa 32000, Israel
[23]Department of Physics and Astronomy, Tel Aviv University, Tel Aviv 69978, Israel
[24]International Centre for Elementary Particle Physics and Department of Physics, University of Tokyo, Tokyo 113-0033, and Kobe University, Kobe 657-8501, Japan
[25]Institute of Physical and Environmental Sciences, Brunel University, Uxbridge, Middlesex UB8 3PH, UK
[26]Particle Physics Department, Weizmann Institute of Science, Rehovot 76100, Israel
[27]Universität Hamburg/DESY, II Institut für Experimental Physik, Notkestrasse 85, D-22607 Hamburg, Germany
[28]University of Victoria, Department of Physics, P O Box 3055, Victoria BC V8W 3P6, Canada
[29]University of British Columbia, Department of Physics, Vancouver BC V6T 1Z1, Canada
[30]University of Alberta, Department of Physics, Edmonton AB T6G 2J1, Canada
[31]Duke University, Dept of Physics, Durham, NC 27708-0305, USA
[32]Research Institute for Particle and Nuclear Physics, H-1525 Budapest, P O Box 49, Hungary
[33]Institute of Nuclear Research, H-4001 Debrecen, P O Box 51, Hungary

[34]Ludwigs-Maximilians-Universität München, Sektion Physik, Am Coulombwall 1, D-85748 Garching, Germany

[a] and at TRIUMF, Vancouver, Canada V6T 2A3
[b] and Royal Society University Research Fellow
[c] and Institute of Nuclear Research, Debrecen, Hungary
[d] and Department of Experimental Physics, Lajos Kossuth University, Debrecen, Hungary
[e] on leave of absence from the University of Freiburg

1 Introduction

A direct search for charginos and neutralinos predicted in SUSY theories [1] is performed using the data collected with the OPAL detector at the centre-of-mass energies ($\sqrt{s}$) of 181–184 GeV at the LEP e^+e^- collider at CERN. At these energies, chargino production cross-sections as large as 3.6 pb for a mass of 85 GeV, together with the collected integrated luminosity of 57 pb^{-1}, lead to excellent discovery potential. This paper describes a chargino and neutralino search using the above data sample and an analysis which is improved relative to the one presented in a previous publication [2].

Previous searches for charginos and neutralinos have been performed by OPAL using data collected near the Z peak (LEP1), at $\sqrt{s}$ =130–136 GeV [3], at 161 GeV [4] and at 170–172 GeV [2], and by the other LEP collaborations [5] [6].

Charginos, $\tilde{\chi}_j^{\pm}$, are the mass eigenstates formed by the mixing of the fields of the fermionic partners of the W boson (winos) and those of the charged Higgs bosons (charged higgsinos). Fermionic partners of the γ, Z, and of the neutral Higgs bosons mix to form mass eigenstates called neutralinos, $\tilde{\chi}_i^0$. In each case, the index j or i is ordered by increasing mass. R-parity [7] conservation is assumed; therefore, the lightest supersymmetric particle (LSP) is stable. The LSP is usually considered to be the lightest neutralino, $\tilde{\chi}_1^0$, although it could be the scalar neutrino, $\tilde{\nu}$, if it is sufficiently light. The LSP is undetected due to its weakly interacting nature. The present analysis is valid for either choice of the LSP. In the Minimal Supersymmetric Standard Model (MSSM) there are two chargino mass eigenstates ($\tilde{\chi}_1^{\pm}$ and $\tilde{\chi}_2^{\pm}$) and four neutralino mass eigenstates ($\tilde{\chi}_1^0$, $\tilde{\chi}_2^0$, $\tilde{\chi}_3^0$ and $\tilde{\chi}_4^0$).

If charginos exist and are sufficiently light, they are pair-produced through a γ or Z in the s-channel. For the wino component there is an additional production process through scalar electron-neutrino ($\tilde{\nu}_e$) exchange in the t-channel. The production cross-section is large unless the scalar neutrino (sneutrino) is light, in which case the cross-section is reduced by destructive interference between the s-channel e^+e^- annihilation to Z or γ and t-channel $\tilde{\nu}_e$ exchange diagrams [8, 9]. The details of chargino decay depend on the parameters of the mixing and the masses of the scalar partners of the ordinary fermions. The lightest chargino $\tilde{\chi}_1^+$ can decay into $\tilde{\chi}_1^0\ell^+\nu$, or $\tilde{\chi}_1^0 q\overline{q}'$, via a W boson, scalar lepton ($\tilde{\ell}$, $\tilde{\nu}$) or scalar quark (squark, $\tilde{q}$). In much of the MSSM parameter space, $\tilde{\chi}_1^+$ decays via a W boson are dominant. Due to the energy and momentum carried away by the LSP (and possibly by neutrinos), the experimental signature for $\tilde{\chi}_1^+\tilde{\chi}_1^-$ events is large missing energy and large missing momentum transverse to the beam axis. If the sneutrino is lighter than the chargino, the two-body decay $\tilde{\chi}_1^+ \to \tilde{\nu}\ell^+$ dominates. Special attention is paid to the case $m_{\tilde{\nu}} \approx m_{\tilde{\chi}_1^{\pm}}$ that would result in two low-momentum charged leptons.

Neutralino pairs ($\tilde{\chi}_1^0\tilde{\chi}_2^0$) can be produced through an s-channel virtual Z, or by t-channel scalar electron (selectron, $\tilde{e}$) exchange [10]. The MSSM prediction for the $\tilde{\chi}_1^0\tilde{\chi}_2^0$ production cross-section can vary significantly depending on the choice of MSSM parameters. It is typically a fraction of a picobarn and generally much lower than the cross-section for $\tilde{\chi}_1^-\tilde{\chi}_1^+$ production. The $\tilde{\chi}_2^0$ will decay into $\tilde{\chi}_1^0\nu\bar{\nu}$, $\tilde{\chi}_1^0\ell^+\ell^-$ or $\tilde{\chi}_1^0 q\bar{q}$, through a $Z^{(*)}$ boson, sneutrino, slepton, squark or a neutral SUSY Higgs boson (h^0 or A^0). The decay via $Z^{(*)}$ is the dominant mode in most of the parameter space. For the cases of $\tilde{\chi}_2^0 \to \tilde{\chi}_1^0\ell^+\ell^-$ or $\tilde{\chi}_1^0 q\bar{q}$, this leads to an experimental signature consisting either of an acoplanar pair of particles or jets, or a monojet if the two jets in the final state have merged. The radiative decay process $\tilde{\chi}_2^0 \to \tilde{\chi}_1^0\gamma$ is also possible [11] and can dominate for some regions of the parameter space.

Motivated by Grand Unification and to simplify the physics interpretation, the Constrained Minimal Supersymmetric Standard Model (CMSSM) [8, 9, 10, 12] is used to guide the analysis but more general cases are also studied. In the CMSSM all the gauginos (SUSY partners of $U(1)_Y$, $SU(2)_L$ and $SU(3)_c$ gauge bosons) are assumed to have a common mass, $m_{1/2}$, at the grand unified (GUT) mass scale, and all the sfermions (SUSY partners of quarks and leptons) have a common mass, m_0, at the GUT mass scale.

In the CMSSM analyses reported here all possible cascade decay processes [10, 12] are taken into account. For example, if $\tilde{\chi}_2^0$ is lighter than $\tilde{\chi}_1^+$, the cascade decay of the chargino, $\tilde{\chi}_1^+ \to \mathrm{f\bar{f}}\tilde{\chi}_2^0, (\tilde{\chi}_2^0 \to \mathrm{f\bar{f}}\tilde{\chi}_1^0$, or $\tilde{\chi}_2^0 \to \gamma\tilde{\chi}_1^0)$, is possible[1]. The production of $\tilde{\chi}_3^0$ is also taken into account in the analysis. The experimental signatures for the $\tilde{\chi}_1^0\tilde{\chi}_3^0$ production are similar to those for $\tilde{\chi}_1^0\tilde{\chi}_2^0$, if $\tilde{\chi}_3^0$ decays into $\tilde{\chi}_1^0\mathrm{Z}^{(*)}$, or into $\tilde{\chi}_1^0\mathrm{h}^0$, $\tilde{\chi}_1^0\mathrm{A}^0$ or $\tilde{\chi}_1^0\gamma$.

This paper is organised as follows. The various event simulations which have been used are described in Section 2. Analyses of the possible signal topologies are discussed in Section 3 and results and physics interpretations, both model independent and based on the CMSSM, are given in Section 4.

2 The OPAL Detector and Event Simulation

2.1 The OPAL Detector

The OPAL detector is described in detail in [14]. It is a multipurpose apparatus having nearly complete solid angle coverage[2]. The central tracking system consists of a silicon microvertex detector, a vertex drift chamber, a jet chamber and z-chambers. In the range $|\cos\theta| < 0.73$, 159 points can be measured in the jet chamber along each track. At least 20 points on a track can be obtained over 96% of the full solid angle. The whole tracking system is located inside a 0.435 T axial magnetic field. A lead-glass electromagnetic (EM) calorimeter providing acceptance within $|\cos\theta| < 0.984$ together with presamplers and time-of-flight scintillators is located both outside the magnet coil and at the front of each endcap. The magnet return yoke is instrumented for hadron calorimetry (HCAL), giving a polar angle coverage of $|\cos\theta| < 0.99$, and is surrounded by external muon chambers. The forward detectors (FD) and silicon-tungsten calorimeters (SW) located on both sides of the interaction point measure the luminosity and complete the geometrical acceptance down to 24 mrad in polar angle. The small gap between the endcap EM calorimeter and FD is filled by an additional electromagnetic calorimeter, called the gamma-catcher (GC).

2.2 Event Simulation

The DFGT generator [15] is used to simulate signal events. It includes spin correlations and allows for a proper treatment of both the W boson and the Z boson width effects in the chargino

[1]Pair production of $\tilde{\chi}_2^0\tilde{\chi}_2^0$ is also possible, but direct searches for this channel with the decays $\tilde{\chi}_2^0 \to \tilde{\chi}_1^0\mathrm{Z}^{(*)}$ would contribute negligibly to the overall limits placed on the CMSSM parameter space, and direct searches for this mode are not made in this analysis. The process $\tilde{\chi}_2^0\tilde{\chi}_2^0 \to \gamma\tilde{\chi}_1^0\gamma\tilde{\chi}_1^0$ is taken into account in the CMSSM limits calculations using the experimental results of another OPAL analysis [13].

[2]A right-handed coordinate system is adopted, where the x-axis points to the centre of the LEP ring, and positive z is along the electron beam direction. The angles θ and ϕ are the polar and azimuthal angles, respectively.

and heavy neutralino decays. The generator includes initial-state radiation and uses the JETSET 7.4 package [16] for the hadronisation of the quark-antiquark system in the hadronic decays of charginos and neutralinos. SUSYGEN [17] is used to calculate the branching fractions for the CMSSM interpretation of the analysis. The most important parameters influencing the chargino detection efficiency are the mass of the lightest chargino, $m_{\tilde{\chi}_1^+}$, and the mass difference between the lightest chargino and the lightest neutralino, $\Delta M_+ \equiv m_{\tilde{\chi}_1^+} - m_{\tilde{\chi}_1^0}$. $\tilde{\chi}_1^+\tilde{\chi}_1^-$ events are generated for 78 points in the ($m_{\tilde{\chi}_1^+}$,ΔM_+) plane, for $m_{\tilde{\chi}_1^+}$ between 50 GeV and 90 GeV and ΔM_+ between 3 GeV and $m_{\tilde{\chi}_1^+}$. At each point 1000 events for the decay $\tilde{\chi}_1^+ \to \tilde{\chi}_1^0 \mathrm{W}^{*+}$ are generated. For the two-body decays of the chargino ($\tilde{\chi}_1^+ \to \tilde{\nu}\ell^+$), 43 points of 1000 events are generated in the ($m_{\tilde{\chi}_1^+}$,$m_{\tilde{\nu}}$) plane, for $m_{\tilde{\chi}_1^+}$ between 45 GeV and 90 GeV and $m_{\tilde{\nu}}$ between 1.5 GeV and $m_{\tilde{\chi}_1^+} - 35$ GeV. For the $\tilde{\chi}_1^0\tilde{\chi}_2^0$ production, $m_{\tilde{\chi}_2^0}$ and $\Delta M_0 \equiv m_{\tilde{\chi}_2^0} - m_{\tilde{\chi}_1^0}$ are the main parameters affecting the efficiency. The $\tilde{\chi}_1^0\tilde{\chi}_2^0$ events are generated in 75 points of the ($m_{\tilde{\chi}_2^0}$,ΔM_0) plane, for $m_{\tilde{\chi}_1^0} + m_{\tilde{\chi}_2^0}$ between 100 GeV and 180 GeV and ΔM_0 between 3 GeV and $m_{\tilde{\chi}_2^0}$. For the cascade decay of $\tilde{\chi}_1^\pm$, 55 points are generated varying $m_{\tilde{\chi}_2^0}, m_{\tilde{\chi}_1^0}$, and the branching fractions for $\tilde{\chi}_1^+ \to \mathrm{f}\bar{\mathrm{f}}\tilde{\chi}_2^0$ and $\tilde{\chi}_2^0 \to \tilde{\chi}_1^0\gamma$.

The sources of background to the chargino and neutralino signals are two-photon, lepton pairs, multihadronic and four-fermion processes. Two-photon processes are the most important background for the case of small ΔM_+ and small ΔM_0 where the visible energy and momentum transverse to the beam direction for signal and two-photon events are comparatively small. The Monte Carlo generators PHOJET [18] (for $Q^2 < 4.5$ GeV^2) and HERWIG [19] (for $Q^2 \geq 4.5$ GeV^2) are used to simulate hadronic events from two-photon processes. The Vermaseren [20] program is used to simulate leptonic two-photon processes ($\mathrm{e^+e^-e^+e^-}$, $\mathrm{e^+e^-\mu^+\mu^-}$ and $\mathrm{e^+e^-\tau^+\tau^-}$). Four-fermion processes are simulated using the grc4f [21] generator, which takes into account all interferences. The dominant contributions are $\mathrm{W^+W^-}$, $\mathrm{We\nu}$, $\gamma^*\mathrm{Z}$ and $\mathrm{ZZ}^{(*)}$ events, which have topologies very similar to that of the signal. Additional samples of $\mathrm{e^+e^-e^+e^-}$, $\mathrm{e^+e^-\mu^+\mu^-}$ and $\mathrm{e^+e^-\tau^+\tau^-}$ processes which are not covered by the Vermaseren program are generated using grc4f. Lepton pairs are generated using the KORALZ [22] generator for $\tau^+\tau^-(\gamma)$ and $\mu^+\mu^-(\gamma)$ events, and the BHWIDE [23] program for $\mathrm{e^+e^-} \to \mathrm{e^+e^-}(\gamma)$ events. Multihadronic ($\mathrm{q\bar{q}}(\gamma)$) events are simulated using PYTHIA [16].

Generated signal and background events are processed through the full simulation of the OPAL detector [24] and the same event analysis chain was applied to the simulated events as to the data.

3 Data Analysis

The analysis is performed on data collected during the 1997 run of LEP at $\sqrt{s}$ =181–184 GeV. The luminosity weighted average[3] of $\sqrt{s}$ is 182.7 GeV.

Data are used from runs in which all the subdetectors relevant to this analysis were fully operational, corresponding to an integrated luminosity of 56.75 ± 0.27 pb^{-1}. The luminosity is measured using small-angle Bhabha scattering events detected in the silicon-tungsten calorimeter.

[3]Most of the data was taken at 182.7 GeV, 3.3% of the data was taken at 183.8 GeV, 6.1% at 181.8 GeV and 0.6% at less than 181.0 GeV. The error of $\sqrt{s}$ from the beam energy uncertainty is 0.03 GeV.

The following preselection cuts are applied to all data to select well measured events: (1) the number of charged tracks is required to be at least two; (2) the event transverse momentum relative to the beam direction is required to be larger than 1.8 GeV; (3) the total energy deposit in each side of the SW, FD and GC detectors has to be smaller than 2, 2 and 5 GeV, respectively; (4) the visible invariant mass of the event has to exceed 2 GeV; (5) the maximum EM cluster energy and the maximum charged track momentum has to be smaller than 130% of the beam energy to reject badly reconstructed events; and (6) the absolute mean of the impact parameters (with respect to the beam spot position) of the reconstructed charged tracks are required to be smaller than 1 cm for the high multiplicity analyses to reject background from beam-gas and beam-wall interactions.

3.1 Detection of Charginos

To obtain optimal performance the event sample is divided exclusively into three categories, motivated by the topologies expected from chargino events. Separate analyses are applied to the preselected events in each category:

(A) $N_{\rm ch} > 4$ and no isolated leptons, where $N_{\rm ch}$ is the number of charged tracks: when both $\tilde{\chi}_1^+$ and $\tilde{\chi}_1^-$ decay hadronically, signal events tend to fall into this category for modest and large values of $\Delta M_+ (\equiv m_{\tilde{\chi}_1^+} - m_{\tilde{\chi}_1^0})$.

(B) $N_{\rm ch} > 4$ and at least one isolated lepton: if only one of the $\tilde{\chi}_1^\pm$ decays leptonically, signal events tend to fall into this category.

(C) $N_{\rm ch} \leq 4$: events tend to fall into this category if ΔM_+ is small or if both charginos decay leptonically.

The isolated lepton selection criteria are similar to those described in Ref. [2]. Electrons are selected if they satisfy either of the two identification methods described in [25, 26] and muons are identified using three methods [27, 28, 29]. The momentum of the electron or muon candidate is required to be larger than 2 GeV. In order to identify a tau lepton, events are reconstructed using the Durham jet algorithm with a jet resolution parameter of 3 GeV^2. A reconstructed jet is identified as a tau decay if there are only one or three charged tracks in the jet, if the momentum sum of the charged tracks is larger than 2.0 GeV, if the invariant mass of the charged particles in the jet is smaller than 1.5 GeV and if the invariant mass of the jet is smaller than 2.0 GeV. The identified lepton is defined to be isolated if the energy within a cone of half-angle 20° around the electron, muon or tau candidate is less than 2 GeV.

The fraction of $\tilde{\chi}_1^+\tilde{\chi}_1^-$ events falling into category (A) is about 35-50% for most ΔM_+ values. This fraction drops to less than 15% if ΔM_+ is smaller than 5 GeV, since the average charged track multiplicity of the events is smaller. Similarly, the fraction of events falling into category (B) is also about 35-50% for most ΔM_+ values and is less than 10% if ΔM_+ is smaller than 5 GeV. When ΔM_+ is smaller than 10 GeV, the fraction of events falling into category (C) is greater than about 50%. If ΔM_+ is larger than 20 GeV, this fraction is about 10%.

Since the chargino event topology mainly depends on the difference between the chargino mass and the lightest neutralino mass, different selection criteria are applied to four ΔM_+ regions:

(I) $\Delta M_+ \leq 10$ GeV,

(II) 10 GeV $< \Delta M_+ \leq m_{\tilde{\chi}_1^+}/2$,

(III) $m_{\tilde{\chi}_1^+}/2 < \Delta M_+ \leq m_{\tilde{\chi}_1^+} - 20$ GeV,

(IV) $m_{\tilde{\chi}_1^+} - 20$ GeV$< \Delta M_+ \leq m_{\tilde{\chi}_1^+}$.

In region I, the main background comes from two-photon processes. Background from four-fermion processes (mainly W^+W^-) can be safely rejected without sacrificing signal detection efficiency. In regions II and III, the main background comes from four-fermion processes (W^+W^-, single W and $\gamma^* Z^{(*)}$). In these regions the background level is modest. In region IV the W^+W^- background is large and dominant. Since the W^+W^- background is very severe in the region of $\Delta M_+ > 85$ GeV where the chargino decays via an on-mass-shell W-boson, a special analysis (allowing relatively high background and demanding higher signal efficiency) is applied to improve the sensitivity to the chargino signal. Overlap between this analysis and the region IV standard analysis is avoided by selecting the analysis which minimises the expected cross-section limit calculated with only the expected background number. This generally results in the special analysis being applied for $m_{\tilde{\chi}_1^+} > 85$ GeV and $\Delta M_+ \gtrsim 85$ GeV. If $m_{\tilde{\nu}}$ is lighter than $\tilde{\chi}_1^+$, the two-body decays of the chargino ($\tilde{\chi}_1^+ \to \tilde{\nu}\ell^+$) may dominate over the three-body decays via a virtual W. A special analysis, optimised for this case, is also performed in category (C).

For each region a single set of cut values is determined which minimises the expected limit on the signal cross-section at 95% C.L. using Ref. [30]. For this procedure, it is assumed that the distribution of observed candidates arises from the expected number of background events and therefore the choice of cuts is independent of the number of candidates actually observed.

The efficiency for an arbitrary choice of $m_{\tilde{\chi}_1^+}$ and $m_{\tilde{\chi}_1^0}$ is obtained by interpolation using a polynomial fit to the efficiencies determined from the Monte Carlo for each category in each ΔM_+ region.

3.1.1 Analysis (A) ($N_{\rm ch} > 4$ without isolated leptons)

For modest and large values of ΔM_+, if both $\tilde{\chi}_1^+$ and $\tilde{\chi}_1^-$ decay hadronically, signal events tend to fall into category (A). The variables used in the selection criteria and their cut values optimised in each ΔM_+ region are listed in Table 1.

After the preselection, the cuts on $E_{\rm fwd}/E_{\rm vis}$, $|\cos\theta_{\rm miss}|$, $|P_z|$ and $|P_z|/E_{\rm vis}$, where $E_{\rm vis}$ is the total visible energy of the event, $E_{\rm fwd}$ is the visible energy in the region of $|\cos\theta| > 0.9$, $\theta_{\rm miss}$ is the polar angle of the missing momentum and P_z is the visible momentum along the beam axis, are applied to reduce background from two-photon and Z^0 radiative return processes. Most of the remaining background from two-photon processes is rejected by the cuts on $P_{\rm t}$ and $P_{\rm t}^{\rm HCAL}$, the transverse momentum of the event measured without using the hadron calorimeter and using the hadron calorimeter, respectively. In region I, the upper cut on $P_{\rm t}^{\rm HCAL}$ is determined from the range of the signal $P_{\rm t}^{\rm HCAL}$ distribution; it reduces the background from W^+W^- and Weν events.

The number of jets ($N_{\rm jet}$) is reconstructed using the Durham jet algorithm with jet resolution parameter $y_{\rm cut} = 0.005$. With the $N_{\rm jet}$ cut, small invariant mass monojet events from the process

Region	I	II	III	IV
$E_{\rm fwd}/E_{\rm vis}$	< 0.2			
$\lvert\cos\theta_{\rm miss}\rvert$	< 0.85			
$\lvert P_z\rvert$ GeV	< 30			
$\lvert P_z\rvert/E_{\rm vis}$	< 0.7			
$P_{\rm t}$ GeV	> 6			
$P_{\rm t}^{\rm HCAL}$ GeV	[6,30]	> 6		
$N_{\rm jet}$	[2,5]		[3,5]	
$\lvert\cos\theta_{\rm j}\rvert$	< 0.90			
$\phi^{\circ}_{\rm acop}$	$> 15(10^*)$		> 15	
if $M_{\rm vis} > 90$, $p_{\rm max}$ GeV	–		< 20	
$M_{\rm vis}$ GeV	< 60	$[5, 80]$	$[5, 130]$	$[5, 150]$
if $N_{\ell'} = 1$ $M_{\rm had'}$ GeV	< 30	< 50	< 60	$\{60, 90\}$
$E_{\ell'}$ GeV	< 30			< 35
E_1 GeV	–	[2,35]	[2,50]	[2,55]
E_2 GeV	–	[2,25]	[2,50]	[2,55]
if $N_{\rm jet} = 3$ $\lvert P_z\rvert$ GeV	–		$< 10^{**}$	
background				
$\gamma\gamma$	0.23	0.11	0.11	0.11
$\ell^+\ell^-(\gamma)$	0.02	0.02	0.01	0.01
$\mathrm{q\bar{q}}(\gamma)$	0.10	0.11	0.40	0.82
4f	0.67	1.09	5.89	8.43
total bkg.	1.01 ± 0.17	1.33 ± 0.16	6.42 ± 0.29	9.38 ± 0.34
observed	1	1	4	7

Table 1: The list of selection criteria for category (A). The numbers of background events expected for the integrated luminosity of 57 pb^{-1}, for various Standard Model processes, and the total number of background events expected as well as the observed number of events in each ΔM_+ region are also listed. If $N_{\rm jet} = 2$, $\phi_{\rm acop}$ is required to be larger than 10° (as indicated by *). $N_{\rm jet} = [2,\ 5]$ means that $2 \leq N_{\rm jet} \leq 5$. $M_{vis} = \{60, 90\}$ means that $M_{vis} < 60$ or $M_{vis} > 90$ GeV. If $N_{\rm jet} = 3$ and $70 < M_{\rm vis} < 95$ GeV in region III and IV, $|P_z|$ is required to be smaller than 10 GeV (as indicated by **). The errors in the total background include only the statistical errors of simulated background events.

$\gamma^*\mathrm{Z}^{(*)} \to \mathrm{q\bar{q}}\nu\bar{\nu}$ are rejected for regions I and II, and background from $\mathrm{q\bar{q}}(\gamma)$ and single W events is reduced in regions III and IV.

After the above cuts, to calculate the acoplanarity angle ($\phi_{\rm acop}$), the events are forced into two jets, again using the Durham jet algorithm. The polar angle of each jet, $\theta_{\rm j}$ (j=1,2), is required to be far from the beam axis. This cut ensures a good measurement of $\phi_{\rm acop}$ and further reduces the background from the $\mathrm{q\bar{q}}(\gamma)$ and two-photon processes. To select signals with

a large amount of missing momentum due to the two invisible neutralinos and to reduce $q\bar{q}(\gamma)$ background, the acoplanarity angle is required to be large. The acoplanarity angle distributions for region II are shown in Fig. 1 before application of this cut.

For events with an observed invariant mass ($M_{\rm vis}$) greater than 90 GeV, a cut is applied on the maximum track momentum ($p_{\rm max}$) in regions III and IV. This cut reduces $W^+W^- \to \ell\nu q\bar{q}'$ events where the lepton ℓ overlaps with a hadronic jet. The $M_{\rm vis}$ cut is optimised for each ΔM_+ region as shown in Table 1. The distributions of the observed invariant mass are shown in Fig. 2 for region II, after the $\phi_{\rm acop}$ cut.

If a lepton (ℓ') is found with an algorithm based on the looser isolation condition described in Ref. [2], the lepton energy $E_{\ell'}$ and the invariant mass calculated without the lepton, $M_{\rm had'}$, must be smaller than the values expected for $W^+W^- \to \ell\nu q\bar{q}'$ events.

The backgrounds from W^+W^- events and single W events are efficiently suppressed by requiring that the highest energy (E_1) and the second highest energy (E_2) of the jets (reconstructed with $y_{\rm cut} = 0.005$) are smaller than the typical jet energy expected for the W^+W^- background. In region III and IV three-jet events with $|P_Z| < 10$ GeV are rejected if $M_{\rm vis}$ is close to the W mass. This cut reduces the $W^+W^- \to \tau\nu q\bar{q}'$ background with small τ decay product energy.

The numbers of background events expected from the four different sources, for each ΔM_+ region, are given in Table 1. Typical detection efficiencies for $\tilde{\chi}_1^+\tilde{\chi}_1^-$ events are shown in Fig. 9a.

A special analysis is applied in the region of $\Delta M_+ \gtrsim 85$ GeV, since the event topology of the signal is very similar to that of $W^+W^- \to 4$ jets. This similarity is due to the small missing momentum taken by the low mass neutralinos. After selecting well contained events with the cuts $|\cos\theta_{\rm miss}| < 0.95$, $E_{\rm fwd}/E_{\rm vis} < 0.25$ and $|P_z| < 30$ GeV, multijet events with large visible energy are selected ($N_{\rm jet} \geq 4$ and $100 < E_{\rm vis} < 170$ GeV). To select a clear 4-jet topology, $y_{34} \geq 0.0075$, $y_{23} \geq 0.04$ and $y_{45} \leq 0.0015$ are required, where $y_{\{n\}\{n+1\}}$ is defined as the minimum $y_{\rm cut}$ value at which the event is reconstructed as having n-jets. If there is a jet which consists of a single γ with energy greater than 50 GeV, events are considered to be $\gamma q\bar{q}g$ and are rejected. The maximum track momentum is required to be smaller than 40 GeV to reduce background from $W^+W^- \to \ell\nu q\bar{q}'$ events where ℓ overlaps with a hadronic jet. The number of selected events is 29, while the number expected from background processes is 24.7±0.5 (0.0 from $\gamma\gamma$, 0.0 from $\ell^+\ell^-(\gamma)$, 6.4 from $q\bar{q}(\gamma)$ and 18.3 from four fermion final states). The signal efficiency is 26–33% for $m_{\tilde{\chi}_1^+} \geq 85$ GeV and $\Delta M_+ \geq 85$ GeV.

3.1.2 Analysis (B) ($N_{\rm ch} > 4$ with isolated leptons)

$\tilde{\chi}_1^+\tilde{\chi}_1^-$ events in which one of the $\tilde{\chi}_1^\pm$ decays leptonically tend to fall into category (B). The variables used in the selection and their cut values in each ΔM_+ region are listed in Table 2. The signal events are selected with the following criteria:

Cuts on $|\cos\theta_{\rm miss}|$ and $E_{\rm fwd}/E_{\rm vis}$ are made to reject background from two-photon processes and $q\bar{q}(\gamma)$ events. Large transverse momenta are then required to further reduce the contribution from two-photon events. The distributions of $P_{\rm t}$ are shown in Fig. 3 after the $|\cos\theta_{\rm miss}|$ cut. To calculate the acoplanarity angle, events are forced into two jets. A large acoplanarity angle of the two jets is then required to further suppress the two-photon background.

In order to reject $W^+W^- \to \ell\nu q\bar{q}'$ background, various cuts are applied: the momentum of isolated leptons should be small enough; the invariant mass of the event calculated excluding

Region	I	II	III	IV
$E_{\rm fwd}/E_{\rm vis}$	< 0.15	< 0.2	< 0.3	
$\lvert\cos\theta_{\rm miss}\rvert$	< 0.9			
$P_{\rm t}$ GeV	> 4	> 5	> 7	> 8
$P_{\rm t}^{\rm HCAL}$ GeV	> 4	> 5	> 7	> 8
$\lvert\cos\theta_{\rm j}\rvert$	< 0.95			
$\phi^{\circ}_{\rm acop}$	> 20		> 15	
$M_{\rm had}$ GeV	< 30	< 60	[5,60]	[5,65]
p_ℓ GeV	< 20	$< 45^{*}$		[4,50]
$M_{\rm vis}$ GeV	< 50	< 80		$< 80^{**}$
background				
$\gamma\gamma$	0.84	0.06	0.06	0.06
$\ell^+\ell^-(\gamma)$	0.02	0.10	0.13	0.18
$\mathrm{q\bar{q}}(\gamma)$	0.00	0.02	0.11	0.11
4f	0.33	1.18	1.27	3.33
total bkg	1.20±0.49	1.36±0.13	1.56±0.14	3.68±0.21
observed	0	1	1	3

Table 2: The list of selection criteria for category (B). The p_ℓ cut for regions II and III (as indicated by $*$) are a function of $M_{\rm had}$ ($p_\ell < 4.5 M_{\rm had}$ if $M_{\rm had} < 10$ GeV, $p_\ell \leq 45$ GeV if $10 \leq M_{\rm had} \leq 50$ GeV, $p_\ell \leq -4.5(M_{\rm had} - 60$ GeV) if $M_{\rm had} > 50$ GeV). The $M_{\rm vis}$ cut in region IV (as indicated by $**$) is only applied if $M_{\rm had} > 55$ GeV. The numbers of background events expected for the integrated luminosity of 57 pb^{-1} for various Standard Model processes and the total number of background events expected as well as the observed number of events in each ΔM_+ region are also listed. The errors in the total background include only the statistical error of simulated background events.

the highest momentum isolated lepton ($M_{\rm had}$) is required to be smaller than the W mass; in the small ΔM_+ region the upper cut value of $M_{\rm had}$ is reduced, since signal events are concentrated only in the small mass region. The distribution of $M_{\rm had}$ after the $\phi_{\rm acop}$ cut is shown in Fig. 4 for region III. As shown in this figure, most of the $\mathrm{W^+W^-}$ background events are rejected. Futhermore, Weν candidate events in which a fake lepton is found in the W$\to \mathrm{q\bar{q}}'$ decay are further reduced by the $M_{\rm vis}$ cut. Typical detection efficiencies for $\tilde{\chi}_1^+\tilde{\chi}_1^-$ events are shown in Fig. 9a.

A special analysis is applied in the region of $\Delta M_+ \gtrsim 85$ GeV due to the large $\mathrm{W^+W^-}$ background. The selection criteria are identical to those in region IV up to the $\phi_{\rm acop}$ cut as listed in the upper part of Table 2. To reject some $\mathrm{W^+W^-} \to \ell\nu\mathrm{q\bar{q}}'$ events, while keeping a good signal efficiency, $M_{\rm had}$ is required to be between 50 and 90 GeV, and $M_{\rm vis}$ to be between 80 and 130 GeV. The invariant mass of the missing four-momentum and the four-momentum of the highest energy isolated lepton must lie between 90 and 130 GeV. The number of observed events with these criteria is 28, while the number of expected background is 31.8±0.6, almost all from four-fermion processes. The signal efficiency is 30–41% for $m_{\tilde{\chi}_1^+} \geq 85$ GeV and $\Delta M_+ \geq 85$ GeV.

3.1.3 Analysis (C) ($N_{\rm ch} \leq 4$)

Events in which both charginos decay leptonically as well as a large fraction of events for small ΔM_+ tend to fall into category (C). This analysis is especially important for the region of $\Delta M_+ \leq 5$ GeV. Because the background varies significantly with ΔM_+ in region I, this region has been split into 2 sub-regions (a,b). The cut variables and the cut values for each region and sub-region are listed in Table 3.

Region	I		II	III	IV
Sub-region	a	b			
$N_{\rm ch}$	[2,4]				
$\Sigma Q_{\rm i}$	0				
$E_{\rm j}$ GeV	> 1.5				
$N_{\rm ch,j}$	≥ 1				
$\lvert Q_{\rm j}\rvert$	≤ 1				
for $\phi^\circ_{\rm acop}$	≤ 70		–		
$a_{\rm t}/E_{\rm beam}$	> 0.030		–		
$P_{\rm t}/E_{\rm beam}$	> 0.030		–		
$\lvert\cos\theta_a\rvert$	< 0.975		–		
for $\phi^\circ_{\rm acop}$	> 70		–		
$P_{\rm t}/E_{\rm beam}$	> 0.040	> 0.050	> 0.075	> 0.095	> 0.100
$\lvert\cos\theta_{\rm miss}\rvert$	< 0.90			< 0.97	
$\Delta\phi_{(\vec{P}_{\rm miss},\mu)}$ rad	> 1.0				
$\lvert\cos\theta_{\rm j}\rvert$	< 0.85		< 0.95	< 0.97	
$\phi^\circ_{\rm acop}$	[20,150]		>20		
$M_{\rm vis}$ GeV	<10.0	<15.0	<30.0	<40.0	<60.0
$E_1/E_{\rm beam}$	< 0.15	< 0.22	< 0.30	< 1.00	
background					
$\gamma\gamma$	1.99	0.68	2.04	1.53	1.31
$\ell^+\ell^-(\gamma)$	0.02	0.03	0.24	0.83	1.50
$\mathrm{q\bar{q}}(\gamma)$	0.00	0.00	0.01	0.01	0.01
4f	0.33	0.50	2.47	14.70	27.04
total bkg.	2.33±0.36	1.21±0.21	4.77±0.38	17.08±0.48	29.86±0.55
observed	2	0	3	8	21

Table 3: The list of selection criteria for category (C). Selection I(a) is specially optimised for the region of $\Delta M_+ \leq 5$ GeV. The numbers of background events expected for the integrated luminosity of 57 pb^{-1} for various Standard Model processes and the total number of background events expected as well as the observed number of events in each ΔM_+ region are also listed. The errors in the total background include only the statistical error of simulated background events.

The net charge of the event must be zero to reject poorly reconstructed events. Since the signal is expected to have a two lepton or two jet topology, the events are split into two jets using the Durham jet algorithm. To ensure that the jet assignment is correct, each jet must

contain at least a charged track ($N_{\mathrm{ch,j}} \geq 1$), have a significant energy (E_{j}) and the magnitude of the sum of the track charges ($|Q_{\mathrm{j}}|$) must not exceed 1. If the acoplanarity angle is small, cuts are applied on the transverse momentum (P_{t}), the transverse momentum perpendicular to the event thrust axis (a_{t}), and $|\cos\theta_a|$ ($\theta_a \equiv \tan^{-1}(a_{\mathrm{t}}/P_z)$). These cuts reduce the background from two-photon processes and lepton pairs. If the acoplanarity angle is large, cuts on P_{t} and $|\cos\theta_{\mathrm{miss}}|$ are applied to reduce the two-photon background and reject events that may have particles escaping detection along the beam line. The P_{t} distributions for the full acoplanarity angle region are shown in Fig. 5 after the cut on the jet charge.

To reduce the background from $\mathrm{e^+e^-}\mu^+\mu^-$ events in which one of the muons is emitted at a small polar angle and is not reconstructed as a good track, events are rejected if there is a track segment in the muon chamber, or a hadron calorimeter cluster at a small polar angle, near the missing momentum direction ($\vec{P}_{\mathrm{miss}}$) in the plane perpendicular to the beam axis. Soft hadronic events from two-photon processes are rejected by cuts on $|\cos\theta_{\mathrm{j}}|$, ϕ_{acop} and M_{vis}. $\mathrm{W^+W^-} \to \ell^+\nu\ell^-\bar{\nu}$ events are rejected by upper cuts on M_{vis} and on the higher energy of the two jets, E_1/E_{beam}. The distributions of E_1/E_{beam} are shown for region II in Fig. 6 after all the other cuts have been applied. The values and ranges for all cuts are given in Table 3. The typical detection efficiencies for $\tilde{\chi}_1^+\tilde{\chi}_1^-$ events are shown in Fig. 9a.

The analysis is especially optimised for the case that both charginos decay leptonically into three particles ($\tilde{\chi}_1^+ \to \ell^+\nu\tilde{\chi}_1^0$). In addition the analysis is designed to have high efficiency in the small ΔM_+ region, where a large fraction of hadronic events fall into category (C). If $m_{\tilde{\nu}}$ is smaller than $m_{\tilde{\chi}_1^+}$, the two-body decays of the chargino ($\tilde{\chi}_1^+ \to \tilde{\nu}\ell^+$) may dominate over the three body decays via a virtual W. The analysis of Ref. [31] especially tuned for acoplanar lepton search is applied in this case.

3.2 Detection of Neutralinos

To obtain optimal performance the event sample is divided exclusively into two categories, motivated by the topologies expected from neutralino events.

(C) $N_{\mathrm{ch}} \leq 4$: the signal events in which $\tilde{\chi}_2^0$ decays into $\tilde{\chi}_1^0\ell^+\ell^-$ tend to fall into this category. When the mass difference between $\tilde{\chi}_2^0$ and $\tilde{\chi}_1^0$ ($\Delta M_0 \equiv m_{\tilde{\chi}_2^0} - m_{\tilde{\chi}_1^0}$) is small, signal events also tend to fall into this category.

(D) $N_{\mathrm{ch}} > 4$: the signal events in which $\tilde{\chi}_2^0$ decays into $\tilde{\chi}_1^0\mathrm{q\bar{q}}$ tend to fall into this category for modest and large values of ΔM_0.

For events with $N_{\mathrm{ch}} \leq 4$ the category (C) cuts of the chargino search are used. Events falling into category (D) have a monojet or di-jet topology and the cuts described below provide better detection-performance for $\tilde{\chi}_1^0\tilde{\chi}_2^0$ detection than would have been obtained using the cuts of category (A) of the chargino search.

The fraction of events falling into category (C) is 10-20% for $\Delta M_0 \geq$20 GeV but increases to about 70% when $\Delta M_0 \leq$5 GeV. The fraction of invisible events due to $\tilde{\chi}_2^0 \to \tilde{\chi}_1^0\mathrm{Z}^{(*)} \to \tilde{\chi}_1^0\nu\bar{\nu}$ decays is 20-30% depending on ΔM_0.

The event shape of $\tilde{\chi}_1^0\tilde{\chi}_2^0$ events mainly depends on the difference between the $\tilde{\chi}_2^0$ mass and the $\tilde{\chi}_1^0$ mass, therefore the selection criteria are optimised for four ΔM_0 regions:

(i) $\Delta M_0 \leq 10$ GeV,

(ii) $10 < \Delta M_0 \leq 30$ GeV,

(iii) $30 < \Delta M_0 \leq 80$ GeV,

(iv) $\Delta M_0 > 80$ GeV.

In regions i and ii, the main sources of background events are two-photon processes and the $\gamma^* Z^{(*)} \to \mathrm{q\bar{q}}\nu\bar{\nu}$ processes. In regions iii and iv, the main sources of background are four-fermion processes ($\mathrm{W^+W^-}$, $\mathrm{We}\nu$ and $\gamma^* Z^{(*)}$). Selection criteria applied for the low-multiplicity events (category (C)) for regions i, ii, iii and iv are identical to those used in the analysis (C) of the chargino search for regions Ia, II, III and IV, respectively (see Table 3). The typical efficiencies for detecting $\tilde{\chi}^0_1\tilde{\chi}^0_2$ events with the $\tilde{\chi}^0_2 \to \tilde{\chi}^0_1 \mathrm{Z}^*$ decay are shown in Fig. 9b.

3.2.1 Analysis (D) ($\mathbf{N_{ch} > 4}$)

In $\tilde{\chi}^0_1\tilde{\chi}^0_2$ events, if the $\tilde{\chi}^0_2$ decays hadronically, events tend to fall into category (D). The variables used in the selection criteria and their cut values are listed in Table 4.

To reduce the background from $\mathrm{e^+e^-} \to \mathrm{Z}\gamma$ and two-photon processes, requirements on θ_{miss}, $E_{\mathrm{fwd}}/E_{\mathrm{vis}}$ and transverse momenta are set. The acoplanarity angle, as defined in the chargino analysis (A), should be large to remove the two-photon and the $\mathrm{q\bar{q}}$ background events. To ensure the reliability of the measurement of ϕ_{acop}, both jets should have a polar angle θ_{j} in the range $|\cos\theta_{\mathrm{j}}| < 0.95$. The acoplanarity angle distribution for region ii after the $|\cos\theta_{\mathrm{j}}|$ cut is shown in Fig. 7. For region iv the ϕ_{acop} cut is loosened with respect to regions i-iii, since the acoplanarity angle of signal events is smaller. On the other hand the $E_{\mathrm{fwd}}/E_{\mathrm{vis}}$ cut is tightened to reduce the $\mathrm{q\bar{q}}$ background.

After these cuts, the remaining background events come predominantly from $\gamma^*\mathrm{Z} \to \mathrm{q\bar{q}}\nu\bar{\nu}$, $\mathrm{W^+W^-} \to \ell\nu\mathrm{q\bar{q}}'$ and $\mathrm{We}\nu \to \mathrm{q\bar{q}}'\mathrm{e}\nu$. Cuts on the visible mass and on the ratio of the visible mass to the visible energy are then applied to reduce the background from $\gamma^* Z \to \mathrm{q\bar{q}}\nu\bar{\nu}$. In regions iii and iv, $d^2_{23} \equiv y_{23}E^2_{\mathrm{vis}} < 30$ GeV^2 is required to select a clear two-jet topology and to reject $\mathrm{W^+W^-} \to \tau\nu\mathrm{q\bar{q}}'$ events. In Fig.8 the d^2_{23} distribution is shown for region iv after all the other cuts. Typical detection efficiencies for $\tilde{\chi}^0_2\tilde{\chi}^0_1$ events are shown in Fig. 9b.

3.3 Systematic errors and corrections

Systematic errors on the number of expected signal events arise from the following sources: the measurement of the integrated luminosity (0.5%), Monte Carlo statistics in the various signal samples, interpolation errors of the efficiencies to arbitrary values of $m_{\tilde{\chi}^+_1}$ and $m_{\tilde{\chi}^0_1}$ (2–10%), modelling of the cut variables in the Monte Carlo simulations[4] (4–10%), errors due to fragmentation uncertainties in hadronic decays ($< 2\%$), the matrix elements leading to different decay parameters ($< 5\%$) and effects of detector calibration ($< 1\%$). The effect of possible trigger inefficiencies has been investigated and found to be negligible.

[4]This is estimated by comparing the efficiencies obtained by shifting each cut variable by the possible shift in the corresponding distribution which still gives agreement between data and Monte Carlo.

Region	i	ii	iii	iv
$E_{\rm fwd}/E_{\rm vis}$	< 0.15		< 0.20	< 0.05
$\lvert\cos\theta_{\rm miss}\rvert$	< 0.8		< 0.9	
$p_{\rm t}$ GeV	> 5		> 7	
$p_{\rm t}^{\rm HCAL}$ GeV	> 5		> 7	
$\lvert\cos\theta_{\rm j}\rvert$	< 0.95			
$\phi^{\circ}_{\rm acop}$	> 20			> 10
$M_{\rm vis}$ GeV	< 12	< 35	< 70	[20,130]
$M_{\rm vis}/E_{\rm vis}$	> 0.3			–
d_{23}^2 GeV^2	–		< 30	
background				
$\gamma\gamma$	1.05	2.15	0.77	0.00
$\ell^+\ell^-(\gamma)$	0.00	0.03	0.07	0.10
$\rm q\bar{q}(\gamma)$	0.01	0.01	0.04	0.07
4f	0.12	1.29	3.18	10.37
total bkg	1.19±0.50	3.49±0.77	4.05±0.51	10.55±0.35
observed	0	1	3	12

Table 4: The list of selection criteria for $\tilde{\chi}_2^0\tilde{\chi}_1^0$ events in category (D). The numbers of background events expected for the integrated luminosity of 57 pb^{-1} for various Standard Model processes and the total number of background events expected as well as the observed number of events in each ΔM_0 region are also listed. The errors in the total background include only the statistical error of simulated background events.

Systematic errors on the expected number of background events are due to Monte Carlo statistics in the simulated background events (as quoted in Tables 1, 2, 3 and 4), uncertainties in the amount of two-photon background which are estimated by fitting the P_t distributions of simulated two-photon events and the data (30%), and uncertainties in the simulation of the four-fermion processes which are estimated by taking the difference between the predictions of the grc4f [21] and the EXCALIBUR [32] generators (17%). The systematic errors due to the modelling of the cut variables in the detector simulation are less than 7%.

The rate of events in which the measured energy in the SW, FD or GC calorimeters, due to noise and beam related background, exceeded the thresholds in the preselection is 4.5% as estimated from random beam crossing events. Since this effect is not modelled in the simulation, it is taken into account by scaling down the integrated luminosity by this amount.

4 Results

4.1 Limits on the $\tilde{\chi}_1^+\tilde{\chi}_1^-$ and $\tilde{\chi}_2^0\tilde{\chi}_1^0$ production cross-sections

Model-independent upper limits are obtained at 95% C.L. on the production cross-sections. This is done for $\tilde{\chi}_1^+\tilde{\chi}_1^-$ assuming the specific decay mode $\tilde{\chi}_1^{\pm} \to \tilde{\chi}_1^0 {\rm W}^{(*)\pm}$ and for $\tilde{\chi}_1^0\tilde{\chi}_2^0$ production assuming the $\tilde{\chi}_2^0 \to \tilde{\chi}_1^0 {\rm Z}^{(*)}$ decay. Exclusion regions are determined from the observed numbers

of events at $\sqrt{s}$ =181–184 GeV[5], the signal detection efficiencies and their uncertainties, and the numbers of background events expected and their uncertainties. To obtain this limit at a given ($m_{\tilde{\chi}_1^+}$, $m_{\tilde{\chi}_1^0}$) or ($m_{\tilde{\chi}_2^0}$, $m_{\tilde{\chi}_1^0}$) point, the independent analyses ((A), (B) and (C) for chargino, (C) and (D) for neutralino) are combined using the likelihood ratio method [33]. This method assigns greater weight to the analysis which has greater sensitivity.

Systematic uncertainties on the efficiencies are incorporated following the method in Ref. [34], and the systematic uncertainties on the number of expected background events are incorporated by numerical integration, assuming Gaussian errors, as suggested in Ref. [34].

Contours of the 95% C.L. upper limits for the $\tilde{\chi}_1^+\tilde{\chi}_1^-$ cross-sections are shown in Fig. 10 assuming the $\tilde{\chi}_1^\pm \to \tilde{\chi}_1^0 \mathrm{W}^{(*)\pm}$ decay with 100% branching fraction. Although these limits do not depend on the details of the SUSY models considered, a "typical" field content of the gauginos is assumed, leading to particular production angular distributions that are subsequently used in estimating detection efficiencies. Differences in detection efficiencies arise from variations in the angular distributions obtained by using different MSSM parameters corresponding to the same mass combination. The variation of the efficiency is observed to be less than 2%. Of the parameters examined, those yielding the lowest efficiency are used. If the cross-section for $\tilde{\chi}_1^+\tilde{\chi}_1^-$ is larger than 0.6 pb and ΔM_+ is between 5 GeV and about 80 GeV, $m_{\tilde{\chi}_1^+}$ is excluded with 95% C.L. up to the kinematic limit, assuming $Br(\tilde{\chi}_1^+ \to \tilde{\chi}_1^0 \mathrm{W}^{(*)+}) = 100\%$.

Similar contours of the upper limits for the $\tilde{\chi}_2^0\tilde{\chi}_1^0$ cross-sections are shown in Fig. 11. If the cross-section for $\tilde{\chi}_2^0\tilde{\chi}_1^0$ is larger than 0.3 pb and ΔM_0 is greater than 10 GeV, $m_{\tilde{\chi}_2^0}$ is excluded up to the kinematic limit at 95% C.L., assuming $Br(\tilde{\chi}_2^0 \to \tilde{\chi}_1^0 \mathrm{Z}^{(*)}) = 100\%$.

4.2 Limits in the MSSM parameter space

The results of the above searches can be interpreted within the framework of the Constrained MSSM (CMSSM). The phenomenology of the gaugino-higgsino sector of the MSSM is mostly determined by the parameters M_2, μ and $\tan\beta$. In the absence of light sfermions and light SUSY Higgs particles, these three parameters are sufficient to describe the chargino and neutralino sectors completely. Within the CMSSM, a large value of the common scalar mass, m_0 (e.g., $m_0 = 500$ GeV) leads to heavy sfermions and therefore to a negligible suppression of the cross-section due to interference from t-channel sneutrino exchange. Chargino decays would then proceed predominantly via a virtual or real W. On the other hand, a light m_0 results in a low value of the mass of the $\tilde{\nu}$, enhancing the contribution of the t-channel exchange diagrams that may have destructive interference with s-channel diagrams, thus reducing the cross-section for chargino pair production. Small values of m_0 also tend to enhance the leptonic branching ratio of charginos, often leading to smaller detection efficiencies. Certain values of m_0 can lead to the condition $m_{\tilde{\nu}} < m_{\tilde{\chi}_1^\pm}$ and result in the two-body decay mode $\tilde{\chi}_1^\pm \to \tilde{\nu}\ell^\pm$ being dominant. The chargino detection efficiency can be small or zero for these decays, particularly when $m_{\tilde{\nu}} \approx m_{\tilde{\chi}_1^\pm}$, leading to severe degradation in sensitivity.

From the input parameters M_2, μ, $\tan\beta$, m_0 and A (the trilinear coupling), masses, production cross-sections and branching fractions are calculated according to the CMSSM [8, 9, 10, 12].

[5]When calculating limits, cross-sections at different $\sqrt{s}$ are estimated by weighting by $\bar{\beta}/s$ in these proportions, where $\bar{\beta}$ is $p_{\tilde{\chi}_1^\pm}/E_{\mathrm{beam}}$ for $\tilde{\chi}_1^+\tilde{\chi}_1^-$ production or $p_{\tilde{\chi}_2^0}/E_{\mathrm{beam}} = p_{\tilde{\chi}_1^0}/E_{\mathrm{beam}}$ for $\tilde{\chi}_2^0\tilde{\chi}_1^0$ production.

For each set of input parameters, the total number of $\tilde{\chi}_1^+\tilde{\chi}_1^-$, $\tilde{\chi}_2^0\tilde{\chi}_1^0$, $\tilde{\chi}_3^0\tilde{\chi}_1^0$ and $\tilde{\chi}_2^0\tilde{\chi}_2^0$ events expected to be observed are calculated using the integrated luminosity, the cross-sections, branching fractions, and the detection efficiencies which depend upon the masses of the chargino, the lightest neutralino and next-to-lightest neutralino. The relative importance of each of the analyses (A)–(D) changes with the leptonic or hadronic branching ratios, and the likelihood ratio method [33] is used to optimally weight each analysis depending on these branching ratios.

Results are presented for two cases: (i) $m_0 = 500$ GeV (i.e., heavy sfermions), and (ii) the value of m_0 that gives the smallest total number of expected chargino and neutralino events taking into account cross-sections, branching ratios, and detection efficiencies for each set of values of M_2, μ, $\tan\beta$. This value of m_0 hence leads to the worst limit at that point, so that the resulting limits are valid for all m_0. Values of m_0 are considered that remain compatible with the current limits on the $\tilde{\nu}$ mass ($m_{\tilde{\nu}_L} > 43$ GeV [35]), and OPAL upper limits on the cross-section for $\tilde{\ell}$ pair production, particularly right-handed smuon and selectron pair production [31]. Particular attention is paid to the region of values of m_0 leading to the critical mass condition $m_{\tilde{\nu}} \approx m_{\tilde{\chi}_1^\pm}$. When $m_{\tilde{\nu}} \leq m_{\tilde{\chi}_1^\pm}$, resulting in a topology of acoplanar leptons and missing momentum, the upper limits on the cross-section for the two-body chargino decay from Ref. [31] are used. The contribution of the cascade decays $\tilde{\chi}_1^+ \to \tilde{\chi}_2^0\mathrm{X}$ followed by $\tilde{\chi}_2^0 \to \tilde{\chi}_1^0\mathrm{Y}$ are also included. The photonic radiative decay $\tilde{\chi}_2^0 \to \tilde{\chi}_1^0\gamma$ leading to single photon topologies from $\tilde{\chi}_2^0\tilde{\chi}_1^0$ production and acoplanar photons with missing energy topologies from $\tilde{\chi}_2^0\tilde{\chi}_2^0$ are taken into account using the 95% C.L. cross-section upper limits on these topologies from the OPAL results of Ref. [13]. In both of these cases, if the relevant product of cross-section and branching ratio for a particular set of MSSM parameters is greater than the measured 95% C.L. upper limit presented in that paper, then that set of parameters is considered to be excluded.

The following regions of the CMSSM parameters are scanned: $0 \leq M_2 \leq 2000$ GeV, $|\mu| \leq 500$ GeV, and $A = \pm M_2$, $\pm m_0$ and 0. The typical scan step is 0.2 GeV. Checks have been made to ensure that the scanned ranges of parameters are large enough that the exclusion regions change negligibly for even larger ranges. No significant dependence on A is observed. The 95% C.L. upper limit on the expected number of events is determined and systematic errors on efficiencies and backgrounds are incorporated as described previously. Figure 12 shows the resulting exclusion regions in the (M_2,μ) plane for $\tan\beta = 1.5$ and 35 with $m_0 \geq 500$ GeV and for all m_0.

The restrictions on the CMSSM parameter space presented here can be transformed into exclusion regions in the ($m_{\tilde{\chi}_1^\pm}$,$m_{\tilde{\chi}_1^0}$) or ($m_{\tilde{\chi}_2^0}$,$m_{\tilde{\chi}_1^0}$) plane. A given mass pair is excluded only if *all* CMSSM parameters in the scan which lead to that same mass pair are excluded at the 95% C.L. The $\tilde{\chi}_1^\pm$ mass limits are summarised in Table 5. In the ($m_{\tilde{\chi}_1^\pm}$,$m_{\tilde{\chi}_1^0}$) plane, Fig. 13 shows the corresponding 95% C.L. exclusion regions for $\tan\beta = 1.5$ and 35.

Figure 14 shows the corresponding 95% C.L. exclusion regions in the ($m_{\tilde{\chi}_2^0}$,$m_{\tilde{\chi}_1^0}$) plane, for $\tan\beta = 1.5$ and 35. Although the neutralino production cross-section is small, our detection efficiencies in the direct neutralino search are high enough, and we have now collected enough integrated luminosity that, for certain SUSY parameters, we should be able to observe them directly rather than their being excluded indirectly through the exclusion of charginos of certain masses. Regions that would be excluded by the direct neutralino searches alone are also shown in Fig. 14 delimited by the white dotted lines. Mass limits on $\tilde{\chi}_1^0$, $\tilde{\chi}_2^0$, and $\tilde{\chi}_3^0$ are summarised in Table 6.

To study the sensitivity of these numerical mass limits, the limits expected from the Standard Model background processes are computed assuming no signal. For chargino mass limits

		$\tan\beta = 1.5$	$\tan\beta = 35$
$m_0 \geq 500$ GeV	$\Delta M_+ \geq 5$ GeV	$m_{\tilde{\chi}_1^+} > 90.0$ GeV	$m_{\tilde{\chi}_1^+} > 90.2$ GeV
	$\Delta M_+ \geq 10$ GeV	$m_{\tilde{\chi}_1^+} > 91.1$ GeV	$m_{\tilde{\chi}_1^+} > 91.2$ GeV
All m_0 (see text)	$\Delta M_+ \geq 5$ GeV	$m_{\tilde{\chi}_1^+} > 69.1$ GeV	$m_{\tilde{\chi}_1^+} > 65.2$ GeV

Table 5: Lower limits at 95% C.L. obtained on the lightest chargino mass.

		$\tan\beta = 1.5$	$\tan\beta = 35$
$m_0 \geq 500$ GeV	No ΔM_0 restriction	$m_{\tilde{\chi}_1^0} > 38.1$ GeV	$m_{\tilde{\chi}_1^0} > 46.4$ GeV
	$\Delta M_0 \geq 10$ GeV	$m_{\tilde{\chi}_2^0} > 63.0$ GeV	$m_{\tilde{\chi}_2^0} > 91.1$ GeV
		$m_{\tilde{\chi}_3^0} > 102.3$ GeV	$m_{\tilde{\chi}_3^0} > 122.1$ GeV
All m_0 (see text)	No ΔM_0 restriction	$m_{\tilde{\chi}_1^0} > 25.4$ GeV	$m_{\tilde{\chi}_1^0} > 36.5$ GeV
	$\Delta M_0 \geq 10$ GeV	$m_{\tilde{\chi}_2^0} > 51.7$ GeV	$m_{\tilde{\chi}_2^0} > 84.8$ GeV
		$m_{\tilde{\chi}_3^0} > 102.1$ GeV	$m_{\tilde{\chi}_3^0} > 124.4$ GeV

Table 6: Lower limits at 95% C.L. obtained on $m_{\tilde{\chi}_1^0}$, $m_{\tilde{\chi}_2^0}$, and $m_{\tilde{\chi}_3^0}$.

close to the kinematic limit, the expected limits differ by less than 0.2 GeV from the observed limit values, while expected mass limits for other values in Table 5 and Table 6 differ by less than 3.0 GeV from the observed values in all cases.

In the "Higgsino region" where M_2 is large, the mass difference ΔM_+ between the chargino and lightest neutralino decreases with increasing M_2, resulting in a drop in detection efficiency. For $\tan\beta = 1.5$, Fig. 15 illustrates the gaugino mass limits in slices of constant M_2 as well as the correspondence of M_2 with mass difference ΔM_+. For $\mu < 0$ the $m_{\tilde{\chi}_1^+}$ limit is above the kinematical boundary of $\tilde{\chi}_1^+\tilde{\chi}_1^-$ production. This is obtained from the interpretation of the results of the direct $\tilde{\chi}_2^0\tilde{\chi}_1^0$ searches. For larger values of $\tan\beta$ the form of the curves are similar, but the difference between the limits for $\mu < 0$ and $\mu > 0$ for a particular gaugino decreases, and the limits are in general between the $\mu < 0$ and $\mu > 0$ curves shown for $\tan\beta = 1.5$.

Figure 16 illustrates the sensitivity of the chargino mass limit to the mass of the sneutrino set by the chosen value of m_0. The dashed line delineates the condition $m_{\tilde{\chi}_1^\pm} = m_{\tilde{\nu}}$ where the $\tilde{\chi}_1^+\tilde{\chi}_1^-$ search fails due to small visible energy. In the region to the right side of the line, charginos will undergo three-body decays which are searched for directly, while on the left side of the line they decay via the two-body mode $\tilde{\chi}^\pm \to \tilde{\nu}\ell^\pm$ and the results of Ref. [31] are applied. In this case the chargino lower mass limit is set mostly by the right-handed slepton limits with some contributions from neutralino production.

Figure 17 shows the dependence of the mass limits on the value of $\tan\beta$. Of particular interest is the absolute lower limit, in the framework of the CMSSM, on the mass of the lightest neutralino of $m_{\tilde{\chi}_1^0} > 30.1$ GeV (24.2 GeV) at 95% C.L. for $m_0 \geq 500$ GeV (all m_0). This has implications on direct searches for the lightest neutralino as a candidate for dark matter. If the lightest neutralino forms dark matter and it is lighter than about 20 GeV, it is difficult to detect it by terrestrial dark matter searches due to the small recoil energy in the material [36]. Since the formulae for couplings and masses in the gaugino sector are symmetric in $\tan\beta$ and $1/\tan\beta$, these results also hold for $\tan\beta < 1$.

5 Summary and Conclusion

A data sample corresponding to an integrated luminosity of 57 pb^{-1} at $\sqrt{s}$ =181–184 GeV, collected with the OPAL detector, has been analysed to search for pair production of charginos and neutralinos predicted by supersymmetric theories. No evidence for these events has been observed. Assuming $m_{\tilde{\chi}_1^\pm} - m_{\tilde{\chi}_1^0} \geq 5$ GeV, the 95% C.L. lower mass limit of the chargino is 90.0 GeV for $\tan\beta = 1.5$ and 90.2 GeV for $\tan\beta = 35$, within the framework of the CMSSM and for the case of a large universal scalar mass ($m_0 \geq 500$ GeV). For all m_0, the 95% C.L. lower mass limit is 69.1 GeV for $\tan\beta = 1.5$ and 65.2 GeV for $\tan\beta = 35$. In certain regions of parameter space, the $m_{\tilde{\chi}_1^\pm}$ limit exceeds the kinematical boundary of the $\tilde{\chi}_1^+\tilde{\chi}_1^-$ production due to the interpretation of the results from the direct $\tilde{\chi}_2^0\tilde{\chi}_1^0$ search. The absolute lower mass limit on the lightest neutralino in the framework of the CMSSM with $m_0 \geq 500$ GeV is 30.1 GeV at 95% C.L., and 24.2 GeV for the worst-case limit with all m_0. This has implications for experimental searches for the lightest neutralino as a dark matter candidate.

Acknowledgements

We particularly wish to thank the SL Division for the efficient operation of the LEP accelerator at all energies and for their continuing close cooperation with our experimental group. We thank our colleagues from CEA, DAPNIA/SPP, CE-Saclay for their efforts over the years on the time-of-flight and trigger systems which we continue to use. In addition to the support staff at our own institutions we are pleased to acknowledge the
Department of Energy, USA,
National Science Foundation, USA,
Particle Physics and Astronomy Research Council, UK,
Natural Sciences and Engineering Research Council, Canada,
Israel Science Foundation, administered by the Israel Academy of Science and Humanities,
Minerva Gesellschaft,
Benoziyo Center for High Energy Physics,
Japanese Ministry of Education, Science and Culture (the Monbusho) and a grant under the Monbusho International Science Research Program,
Japanese Society for the Promotion of Science (JSPS),
German Israeli Bi-national Science Foundation (GIF),
Bundesministerium für Bildung, Wissenschaft, Forschung und Technologie, Germany,
National Research Council of Canada,
Research Corporation, USA,
Hungarian Foundation for Scientific Research, OTKA T-016660, T023793 and OTKA F-023259.

References

[1] Y. Gol'fand and E. Likhtam, JETP Lett. **13** (1971) 323;
D. Volkov and V. Akulov, Phys. Lett. **B46** (1973) 109;
J. Wess and B. Zumino, Nucl. Phys. **B70** (1974) 39.

[2] OPAL Collab., K. Ackerstaff *et al.*, Euro. Phys. J. **C2** (1998) 213.

[3] OPAL Collab., G. Alexander *et al.*, Phys. Lett. **B377** (1996) 181.

[4] OPAL Collab., K. Ackerstaff *et al.*, Phys. Lett. **B389** (1996) 616.

[5] ALEPH Collab., D. Buskulic *et al.*, Phys. Lett. **B373** (1996) 246;
DELPHI Collab., P. Abreu *et al.*, Phys. Lett. **B382** (1996) 323;
L3 Collab., M. Acciarri *et al.*, Phys. Lett. **B377** (1996) 289.

[6] ALEPH Collab., R. Barate *et al.*, Euro. Phys. J. **C2** (1998) 417;
DELPHI Collab., P. Abreu *et al.*, Euro. Phys. J. **C1** (1998) 1;
L3 Collab., M. Acciarri *et al.*, CERN preprint CERN-PPE/97-130 (1997).

[7] P. Fayet, ' Unification of the Fundamental Particle Interactions', Plenum Press (1980) 587.

[8] A. Bartl, H. Fraas and W. Majerotto, Z. Phys. **C30** (1986) 441;
A. Bartl, H. Fraas and W. Majerotto, Z. Phys. **C41** (1988) 475;
A. Bartl, H. Fraas, W. Majerotto and B. Mösslacher, Z. Phys. **C55** (1992) 257.

[9] M. Chen, C. Dionisi, M. Martinez and X. Tata, Phys. Rep. **159** (1988) 201;
J. L. Feng and M. J. Strassler, Phys. Rev. **D51** (1995) 4661.

[10] A. Bartl, H. Fraas and W. Majerotto, Nucl. Phys. **B278** (1986) 1;
S. Ambrosanio and B. Mele, Phys. Rev. **D52** (1995) 3900.

[11] H. Haber and D. Wyler, Nucl. Phys. **B323** (1989) 267;
H. Komatsu and J. Kubo, Phys. Lett. **B157** (1985) 90 and **B162** (1985) 379.

[12] M. Carena, J.R. Espinosa, M. Quiros and C.E.M. Wagner, Phys. Lett. **B355** (1995) 209.

[13] OPAL Collab., K. Ackerstaff *et al.*, CERN preprint CERN-PPE/97-132, Eur. Phys. Journal **C2** (1998) 607.

[14] OPAL Collab., K. Ahmet *et al.*, Nucl. Instr. Meth. **A305** (1991) 275;
S. Anderson *et al.*, Nucl. Instr. Meth. **A403** (1998) 326;
B.E. Anderson *et al.*, IEEE Trans. on Nucl. Science **41** (1994) 845.

[15] C. Dionisi *et al.*, in 'Physics at LEP2', eds. G. Altarelli, T. Sjöstrand and F. Zwirner, CERN 96-01, vol.2 (1996) 337.

[16] T. Sjöstrand, Comp. Phys. Comm. **82** (1994) 74;
T. Sjöstrand, Lund University report LU TP 95-20.

[17] E. Accomando *et al.*, 'Event Generators for Discovery Physics', hep-ph/9602203, Feb. 1996, and in 'Physics at LEP2', eds. G. Altarelli, T. Sjöstrand and F. Zwirner, CERN 96-01, vol.2 (1996) 299.

[18] E. Boudinov *et al.*, '$\gamma\gamma$ Event Generators', hep-ph/9512371, Dec. 1995, and in 'Physics at LEP2', eds. G. Altarelli, T. Sjöstrand and F. Zwirner, CERN 96-01, vol.2 (1996) 187.

[19] G. Marchesini *et al.*, Comp. Phys. Comm. **67** (1992) 465.

[20] J.A.M. Vermaseren, Nucl. Phys. **B229** (1983) 347.

[21] J. Fujimoto *et al.*, Comp. Phys. Comm. **100** (1997) 128.

[22] S. Jadach, B.F.L. Ward and Z. Wąs, Comp. Phys. Comm. **79** (1994) 503.

[23] S. Jadach, W. Płaczek and B.F.L. Ward, in 'Physics at LEP2', eds. G. Altarelli, T. Sjöstrand and F. Zwirner, CERN 96-01, vol. 2 (1996) 286.

[24] J. Allison *et al.*, Nucl. Instr. Meth. **A317** (1992) 47.

[25] OPAL Collab., R. Akers *et al.*, Phys. Lett. **B327** (1994) 411.

[26] OPAL Collab., R. Akers *et al.*, Z. Phys. **C65** (1994) 17.

[27] OPAL Collab., P. Acton *et al.*, Z. Phys. **C58** (1993) 523.

[28] OPAL Collab., R. Akers *et al.*, Z. Phys. **C60** (1993) 199.

[29] OPAL Collab., G. Alexander *et al.*, Z. Phys. **C52** (1991) 175.

[30] R.M. Barnett *et al.* (Particle Data Group), Phys. Rev. **D54** (1996) Eq. (28.40).

[31] OPAL Collab., K. Ackerstaff *et al.*, CERN-EP/98-122, submitted to Euro. Phys. J. **C**.

[32] F.A. Berends, R. Pittau and R. Kleiss, Comp. Phys. Comm. **85** (1995) 437.

[33] A.G. Frodesen, O. Skeggestad, and H. Tofte, 'Probability and Statistics in Particle Physics', Universitetsforlaget, 1979, ISBN 82-00-01-01906-3;
S.L. Meyer, 'Data Analysis for Scientists and Engineers', John Wiley and Sons, 1975, ISBN 0-471-59995-6.

[34] R.D. Cousins and V.L. Highland, Nucl. Instr. Meth. **A320** (1992) 331.

[35] C. Caso *et al.* (Particle Data Group), Euro. Phys. J. **C3** (1998) 1.

[36] G.G. Raffelt, 'Dark Matter: Motivation, Candidates and Search', in Proceedings of the 1997 European school of High-Energy Physics, e-print hep-ph/9712538;
H.V. Klapdor-Kleingrothaus and A. Staudt, 'Non-accelerator Particle Physics', IOP Publishing Ltd. (1995) pp. 384–416;
W. Ootani *et al.*, preprint RESCEU-35/97, e-print hep-ex/9709019.

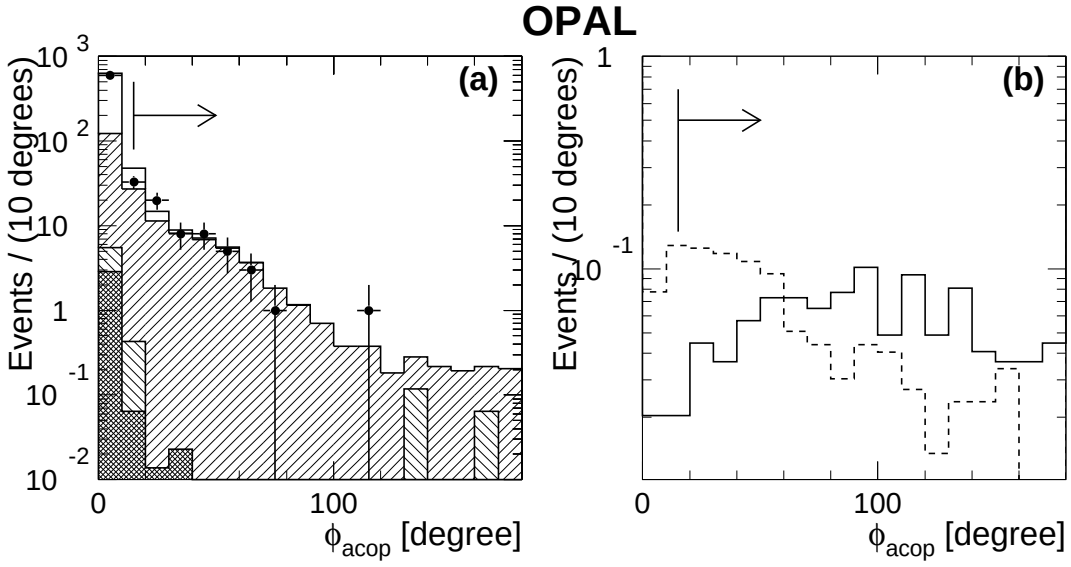

Figure 1: The distributions of the acoplanarity angle, $\phi_{\rm acop}$, in analysis (A) region II. In (a) are shown the data distribution (dark circles) and the predicted contributions from background processes: dilepton events (double hatched area), two-photon processes (negative slope hatched area), four-fermion processes (including W-pair events) (positive slope hatched area), and multihadronic events (open area). In each case the distribution has been normalised to 57 pb^{-1}. In (b) predictions from simulated chargino events are shown for $m_{\tilde{\chi}_1^\pm} = 90$ GeV and $m_{\tilde{\chi}_1^0} = 70$ GeV (solid line histogram) and for $m_{\tilde{\chi}_1^\pm} = 90$ GeV and $m_{\tilde{\chi}_1^0} = 45$ GeV (dashed line histogram). The normalisations of the signal distributions are arbitrary. The arrows shown indicate the selection criteria.

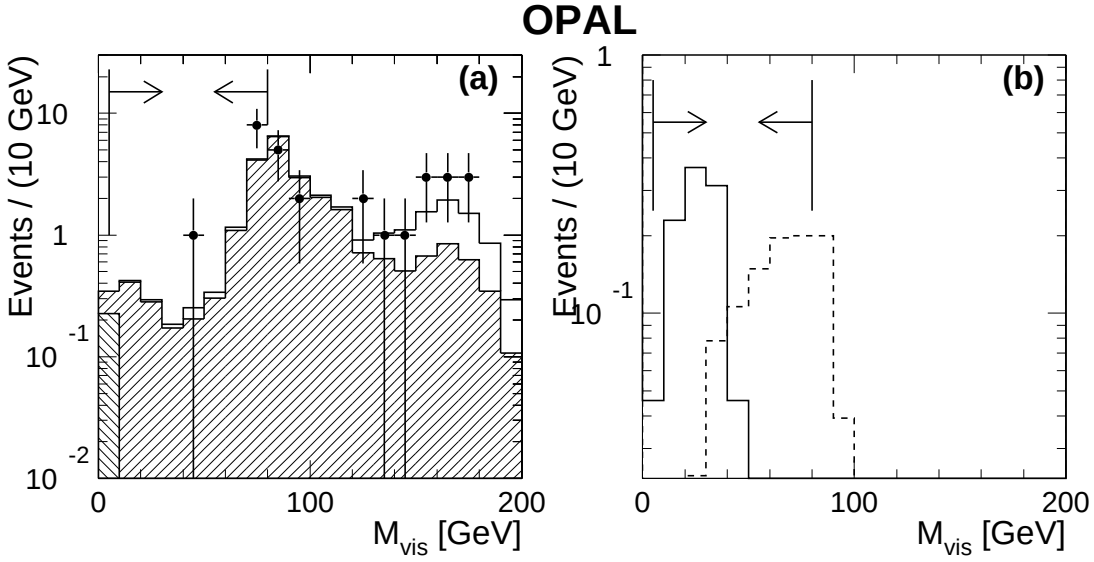

Figure 2: The distributions of $M_{\rm vis}$ in analysis (A) for data and simulated background events are shown in (a) after the $\phi_{\rm acop}$ cut for region II. The background sources are shaded as in Fig.1. Distributions of chargino signal events are shown in (b) for $m_{\tilde{\chi}_1^\pm} = 90$ GeV and $m_{\tilde{\chi}_1^0} = 70$ GeV (solid line) and for $m_{\tilde{\chi}_1^\pm} = 90$ GeV and $m_{\tilde{\chi}_1^0} = 45$ GeV (dashed line). The normalisations of the signal distributions are arbitrary. The arrows shown indicate the selection criteria.

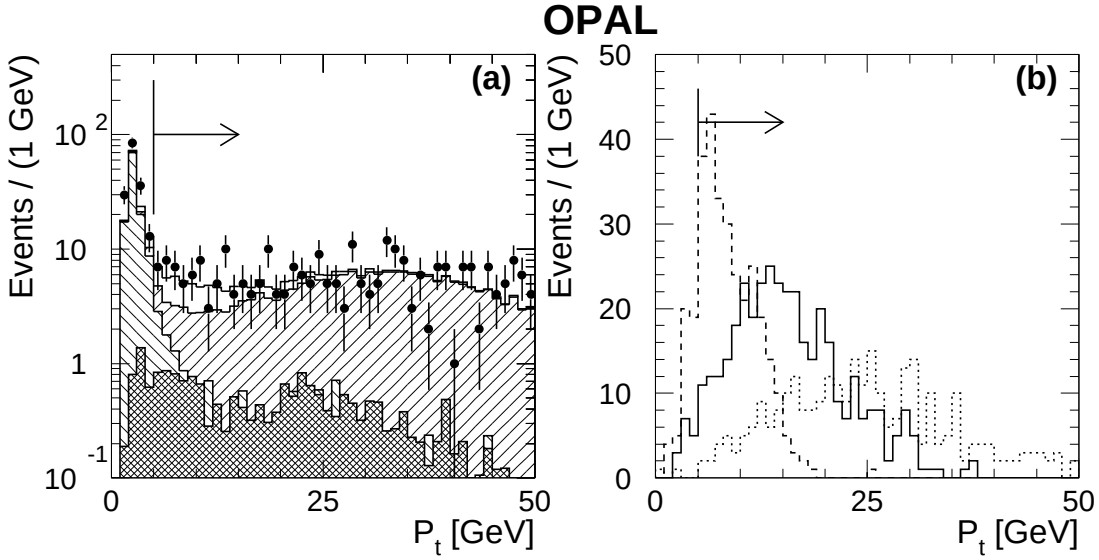

Figure 3: The distributions of P_t in analysis (B) region II after the $|\cos\theta_{\rm miss}|$ cut. Data and expected background contributions are shown in (a). The background sources are shaded as in Fig.1. The distributions of the signal for simulated chargino events with $m_{\tilde{\chi}_1^+} = 90$ GeV and $m_{\tilde{\chi}_1^0} = 70$ GeV (solid histogram), with $m_{\tilde{\chi}_1^+} = 90$ GeV and $m_{\tilde{\chi}_1^0} = 80$ GeV (dashed histogram) and with $m_{\tilde{\chi}_1^+} = 90$ GeV and $m_{\tilde{\chi}_1^0} = 45$ GeV (dotted histogram) are shown in (b). The normalisations of the signal distributions are arbitrary. The arrows shown indicate the selection criteria.

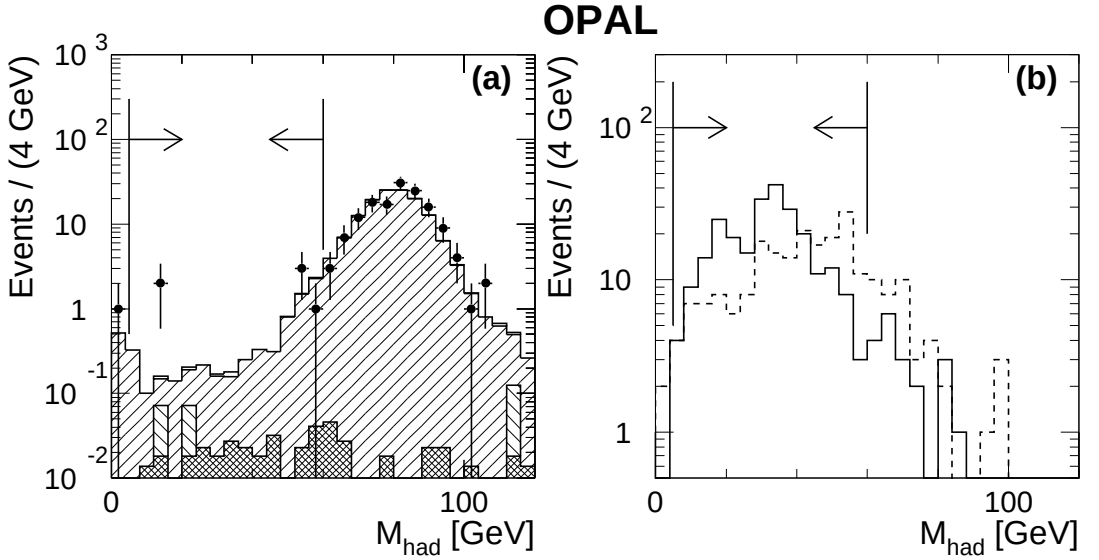

Figure 4: $M_{\rm had}$ distributions in analysis (B) region III after the $\phi_{\rm acop}$ cut. Figure (a) shows the data and the Monte Carlo prediction for background processes. The background sources are shaded as in Fig. 1. The distributions of the signal for simulated chargino events with $m_{\tilde{\chi}_1^+} = 90$ GeV and $m_{\tilde{\chi}_1^0} = 45$ GeV (solid histogram) and with $m_{\tilde{\chi}_1^+} = 90$ GeV and $m_{\tilde{\chi}_1^0} = 20$ GeV (dashed histogram) are shown in (b). The normalisations of the signal distributions are arbitrary. The arrows shown indicate the selection criteria.

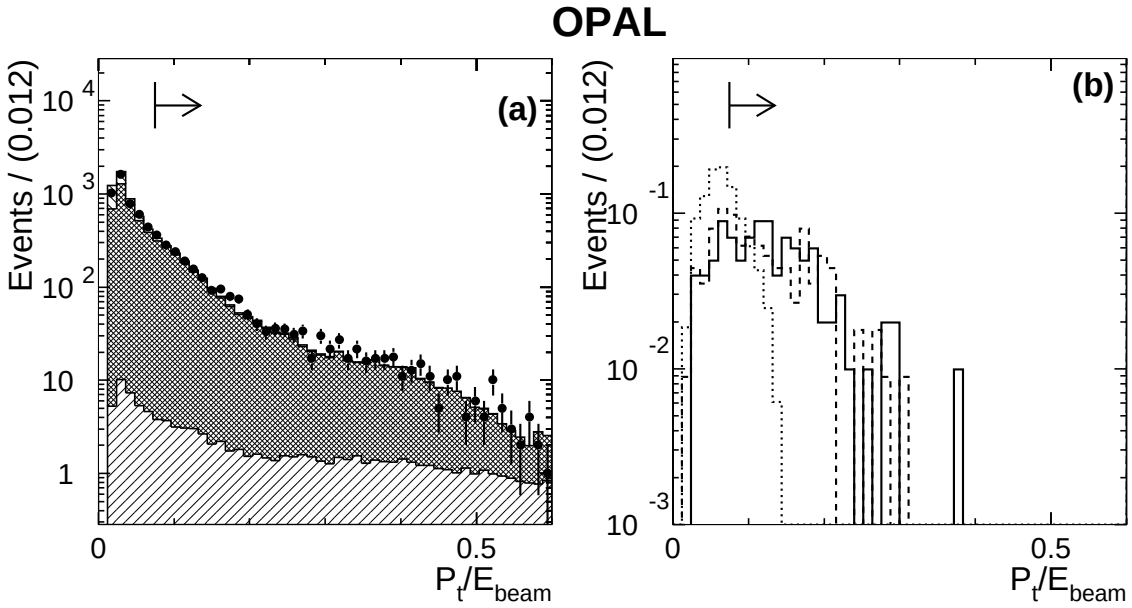

Figure 5: The distributions of $P_t/E_{\rm beam}$ after the cut on the jet charge for events in analysis (C) region II. Data and background contributions are shown in (a). The background sources are shaded as in Fig. 1. In (b) predictions from the simulation for chargino and neutralino events are shown: $m_{\tilde{\chi}_1^+} = 90$ GeV and $m_{\tilde{\chi}_1^0} = 70$ GeV (solid line), $m_{\tilde{\chi}_1^+} = 90$ GeV and $m_{\tilde{\chi}_1^0} = 45$ GeV (dashed line) and $m_{\tilde{\chi}_2^0} = 95$ GeV and $m_{\tilde{\chi}_1^0} = 85$ GeV (dotted line). The normalisations of the signal distributions are arbitrary. The arrows shown indicate the selection criteria.

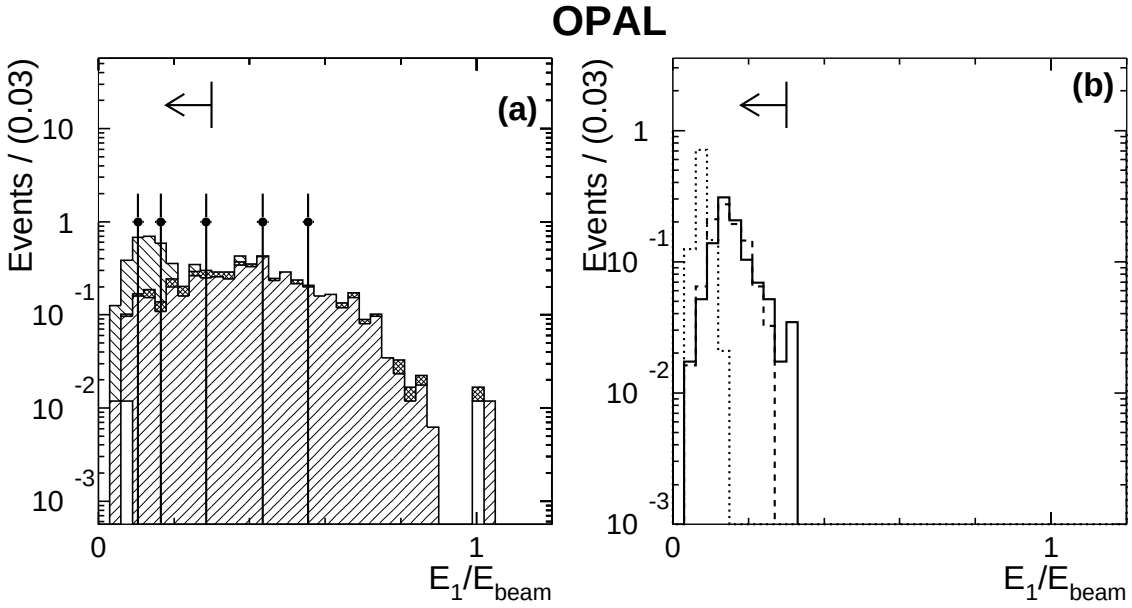

Figure 6: Distributions of the highest jet energy in analysis (C) region II after all other cuts have been applied. Data and background contributions are shown in (a). The background sources are shaded as in Fig. 1. The Monte Carlo signal distributions are shown in (b) and are labelled as in Fig. 5. The normalisations of the signal distributions are arbitrary. The arrows shown indicate the selection criteria.

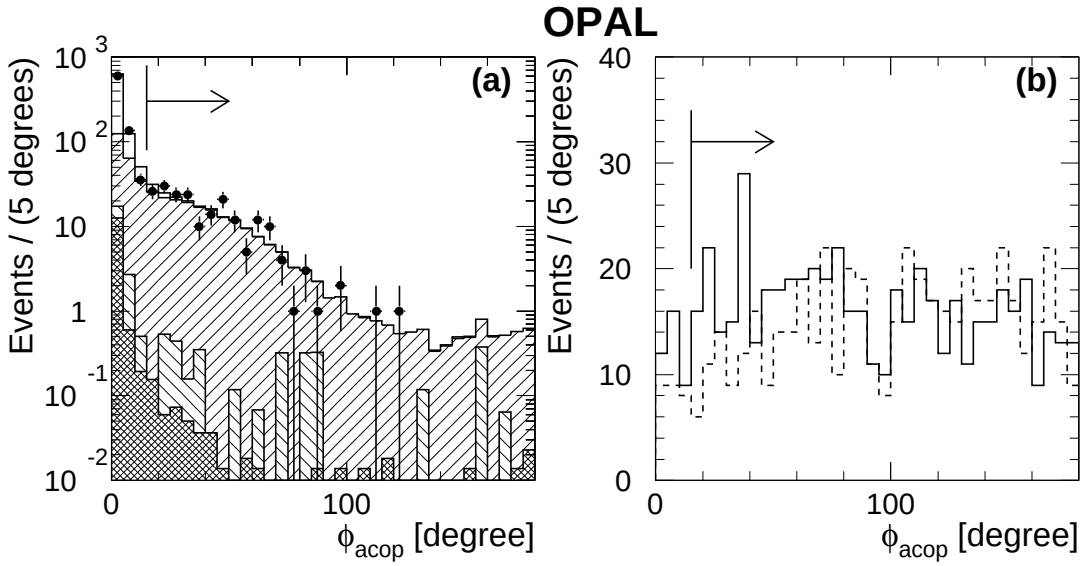

Figure 7: The distributions of acoplanarity angle in analysis (D) region ii after cut on P_t. Data and background contributions are shown in (a). The background sources are shaded as in Fig. 1. The Monte Carlo signal distributions are shown in (b) for $m_{\tilde{\chi}^0_2} = 105$ GeV and $m_{\tilde{\chi}^0_1} = 75$ GeV (solid line) and for $m_{\tilde{\chi}^0_2} = 100$ GeV and $m_{\tilde{\chi}^0_1} = 80$ GeV (dashed line). The normalisations of the signal distributions are arbitrary. The arrows shown indicate the selection criteria.

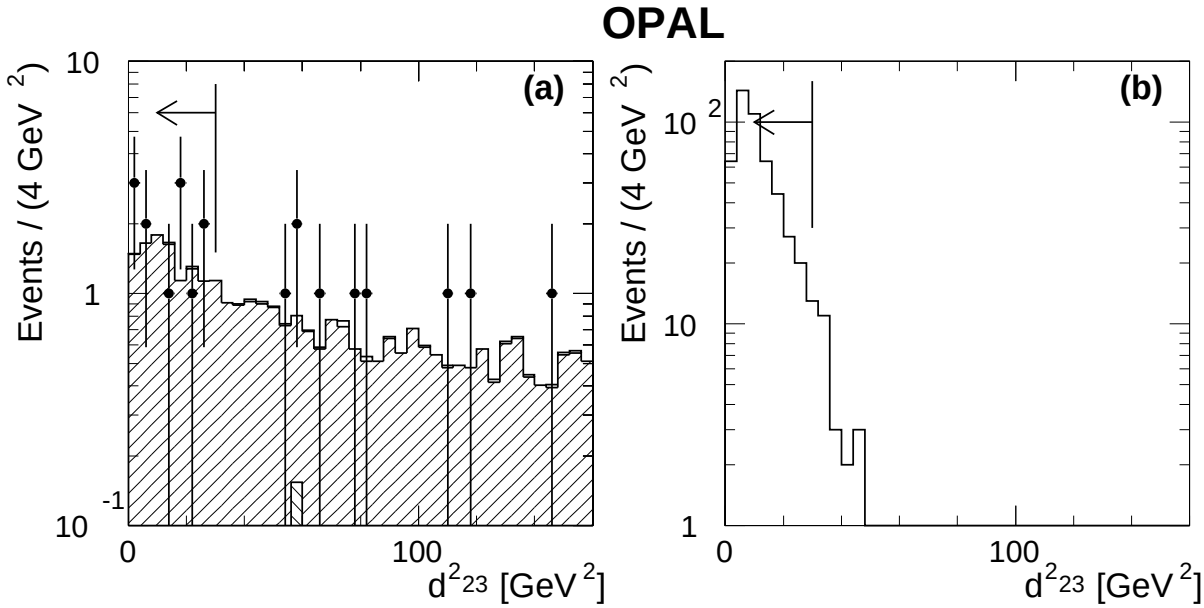

Figure 8: The distributions of $d_{23}(\equiv y_{23}E^2_{\rm vis})$ GeV^2 in analysis (D) region iv for three jet events after all the other cuts. Data and background contributions are shown in (a). The background sources are shaded as in Fig. 1. The Monte Carlo signal distribution is shown in (b) for $m_{\tilde{\chi}^0_2} = 150$ GeV and $m_{\tilde{\chi}^0_1} = 20$ GeV. The normalisation of the signal distribution is arbitrary. The arrows shown indicate the selection criteria.

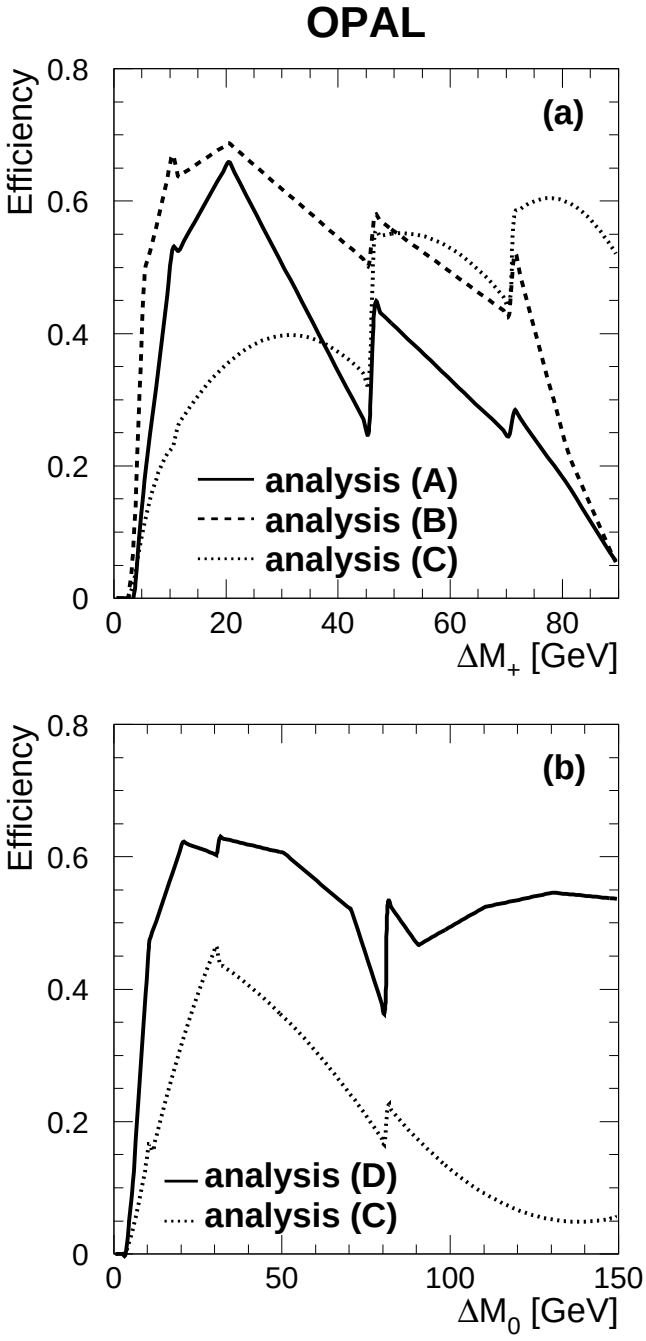

Figure 9: (a) Detection efficiencies of analyses (A) (solid line), (B) (dashed line) and (C) (dotted line) for $\tilde{\chi}_1^+\tilde{\chi}_1^-$ events as a function of $\Delta M_+ \equiv m_{\tilde{\chi}_1^+} - m_{\tilde{\chi}_1^0}$, for $m_{\tilde{\chi}_1^+} = 90$ GeV. (b) Detection efficiencies of analyses (C) (dotted line) and (D) (solid line) for $\tilde{\chi}_1^0\tilde{\chi}_2^0$ events as a function of $\Delta M_0 \equiv m_{\tilde{\chi}_2^0} - m_{\tilde{\chi}_1^0}$, for $m_{\tilde{\chi}_1^0} + m_{\tilde{\chi}_2^0} = 170$ GeV. The efficiencies for each analysis are normalised to the number of events in each category.

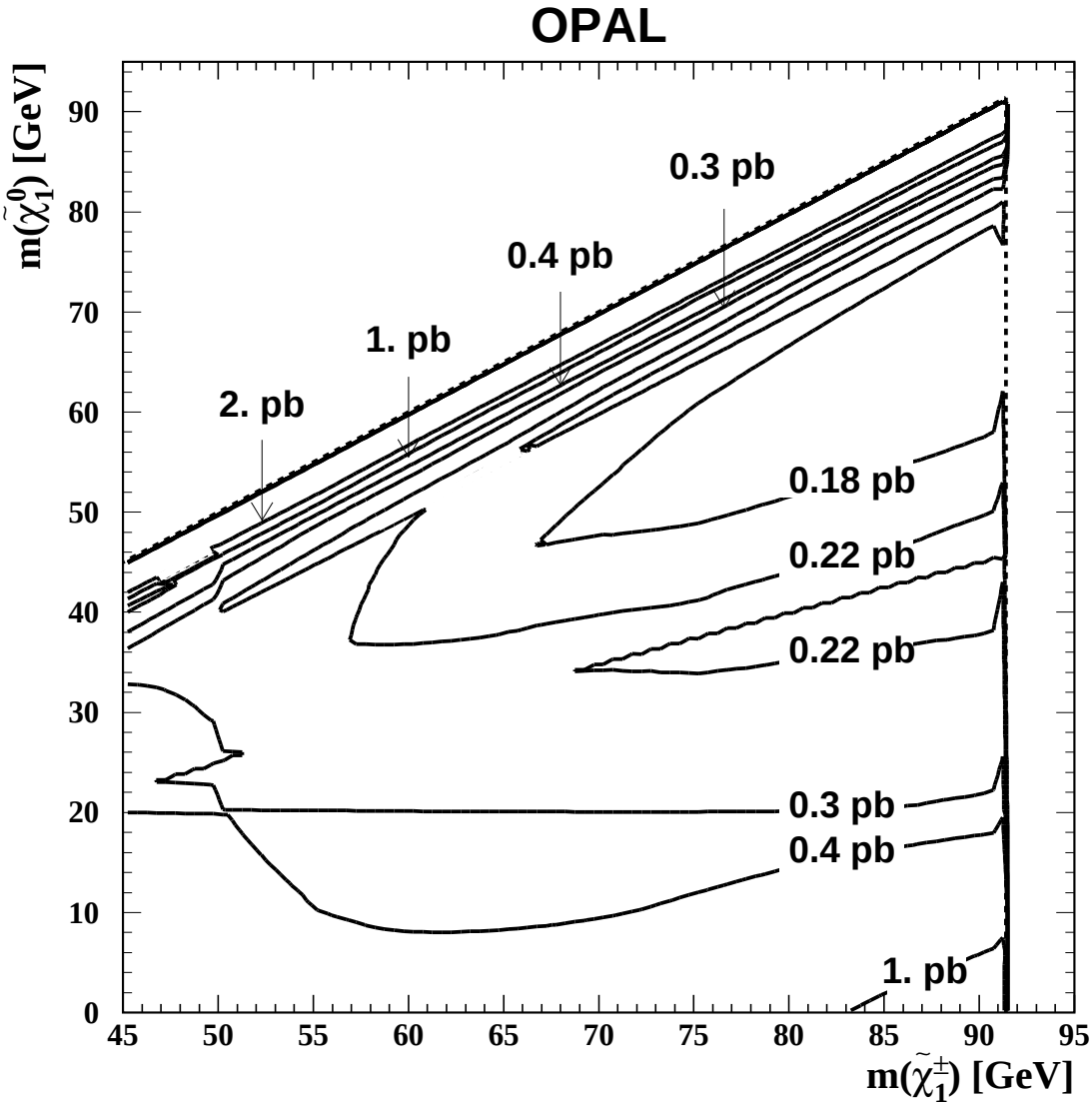

Figure 10: The contours of the 95% C.L. upper limits for the $e^+e^- \to \tilde{\chi}_1^+\tilde{\chi}_1^-$ production cross-sections at $\sqrt{s} = 182.7$ GeV are shown assuming $Br(\tilde{\chi}_1^+ \to \tilde{\chi}_1^0 W^{(*)+}) = 100\%$.

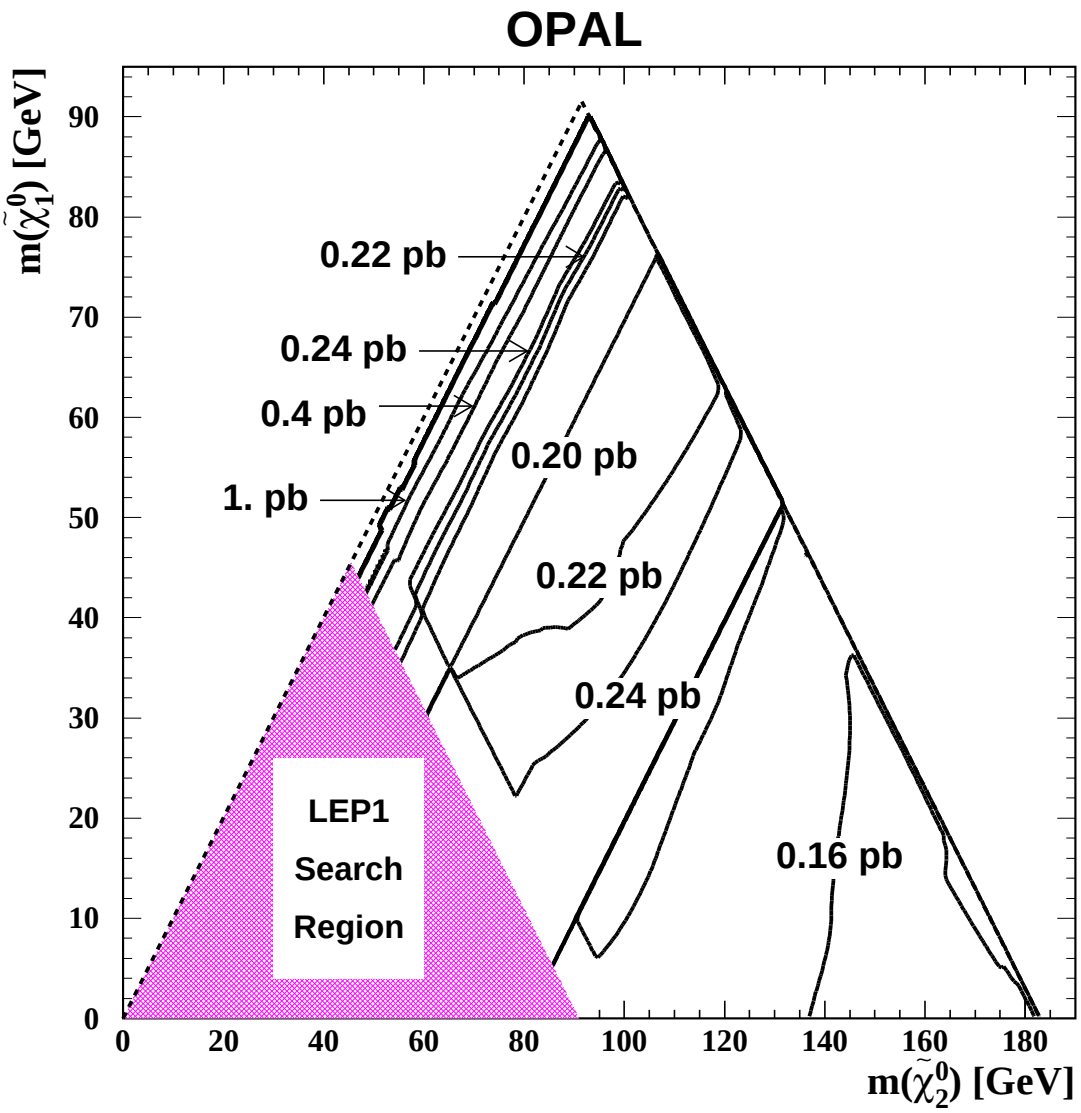

Figure 11: The contours of the 95% C.L. upper limits for the $e^+e^- \to \tilde{\chi}_2^0\tilde{\chi}_1^0$ production cross-sections at $\sqrt{s} = 182.7$ GeV are shown assuming $Br(\tilde{\chi}_2^0 \to \tilde{\chi}_1^0 Z^{(*)}) = 100\%$. The region for which $m_{\tilde{\chi}_2^0} + m_{\tilde{\chi}_1^0} < m_Z$ is not considered in this analysis.

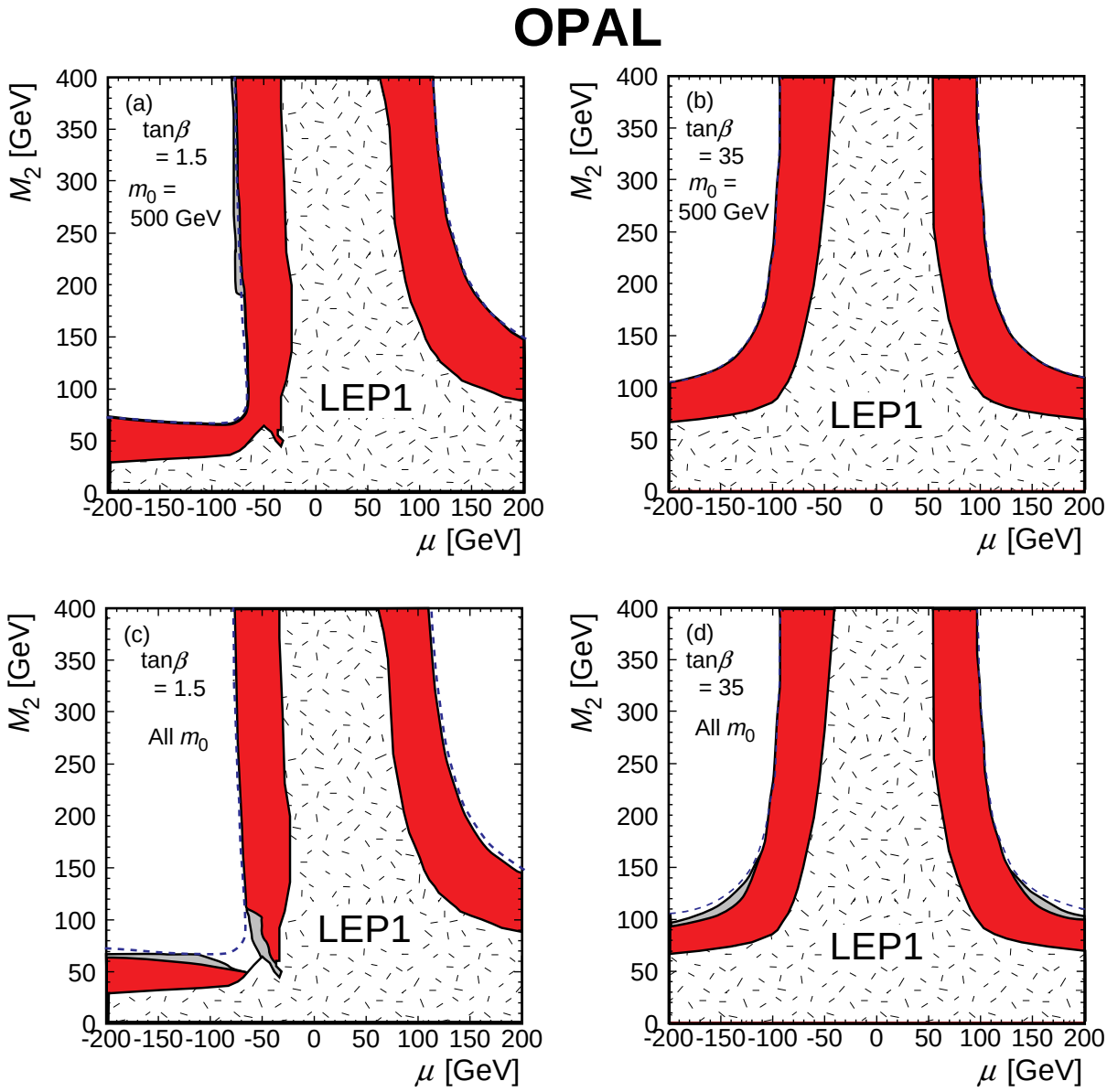

Figure 12: Exclusion regions at 95% C.L. in the (M_2,μ) plane with $m_0 \geq 500$ GeV for (a) $\tan\beta = 1.5$ and for (b) $\tan\beta = 35$. Exclusion regions valid for all m_0 for (c) $\tan\beta = 1.5$ and for (d) $\tan\beta = 35$. The speckled areas show the LEP1 excluded regions and the dark shaded areas show the additional exclusion region using the data from $\sqrt{s} = 181$–184 GeV. The kinematical boundaries for $\tilde{\chi}_1^+\tilde{\chi}_1^-$ production are shown by the dashed curves. The light shaded region in (a) extending beyond the kinematical boundary of the $\tilde{\chi}_1^+\tilde{\chi}_1^-$ production is obtained due to the interpretation of the results from the direct neutralino searches. The light shaded regions elsewhere show the additional exclusion regions due to direct neutralino searches and other OPAL search results (see text).

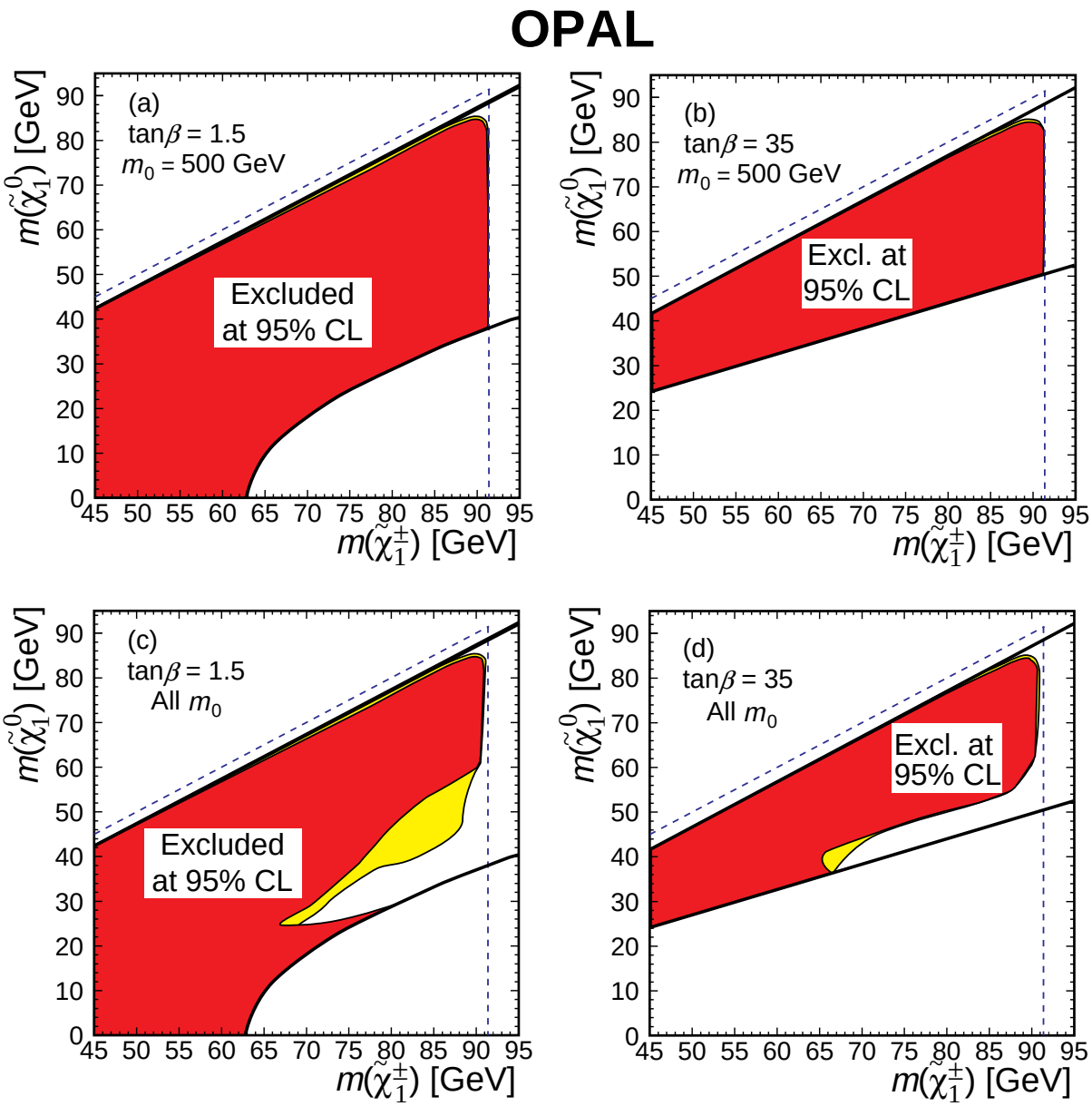

Figure 13: The 95% C.L. excluded region in the $(m_{\tilde{\chi}_1^0}, m_{\tilde{\chi}_1^+})$ plane within the framework of the CMSSM with $m_0 \geq 500$ GeV for (a) $\tan\beta = 1.5$ and for (b) $\tan\beta = 35$. The excluded region valid for all m_0 for (c) $\tan\beta = 1.5$ and for (d) $\tan\beta = 35$. The thick solid lines represent the theoretical bounds of the CMSSM parameter space as given in the text. The kinematical boundaries for $\tilde{\chi}_1^+\tilde{\chi}_1^-$ production and decay at $\sqrt{s} = 182.7$ GeV are shown by dashed lines. The light shaded areas show the additional exclusion regions due to direct neutralino searches and other OPAL search results (see text).

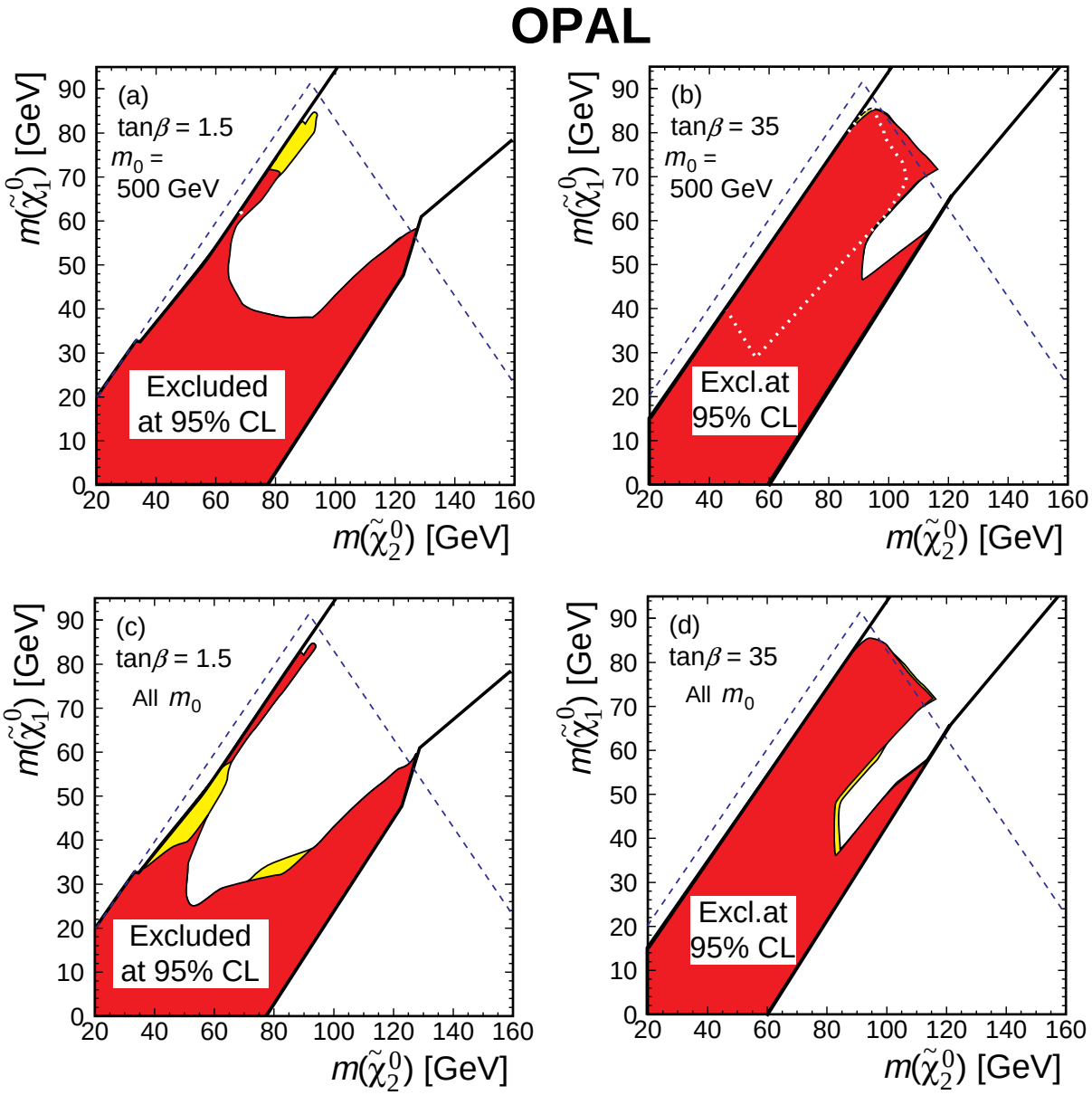

Figure 14: The 95% C.L. excluded region in the $(m_{\tilde{\chi}^0_1}, m_{\tilde{\chi}^0_2})$ plane within the framework of the CMSSM with $m_0 \geq 500$ GeV for (a) $\tan\beta = 1.5$ and for (b) $\tan\beta = 35$. The excluded region valid for all m_0 for (c) $\tan\beta = 1.5$ and for (d) $\tan\beta = 35$. The thick solid lines represent the theoretical bounds of the CMSSM parameter space as defined in the text. The kinematical boundaries for $\tilde{\chi}^0_2\tilde{\chi}^0_1$ production and decay at $\sqrt{s} = 183$ GeV are shown by dashed lines. The regions excluded outside of the kinematical boundary $m_{\tilde{\chi}^0_2} + m_{\tilde{\chi}^0_1} = \sqrt{s}$ is due to the interpretation of the $\tilde{\chi}^+_1\tilde{\chi}^-_1$ search results. The dark region is excluded by the results of direct $\tilde{\chi}^+_1\tilde{\chi}^-_1$ searches. The light shaded areas show the additional exclusion regions due to direct neutralino searches and other OPAL search results (see text). The regions inside the white dotted lines in Fig.(a) and (b) would be excluded by the direct neutralino searches alone.

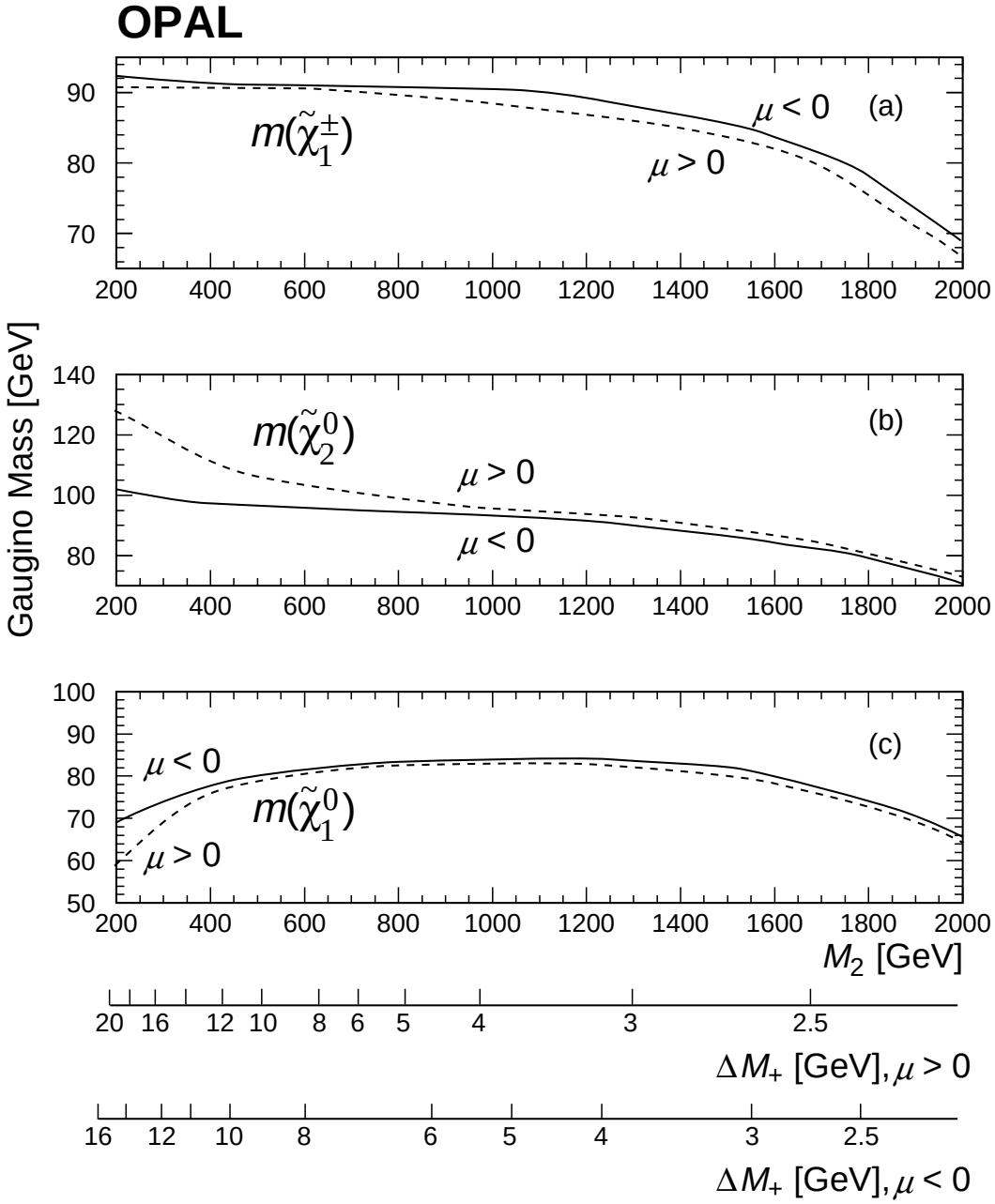

Figure 15: The 95% C.L. lower mass limits for (a) $\tilde{\chi}_1^+$, (b) $\tilde{\chi}_2^0$, and (c) $\tilde{\chi}_1^0$ for $\tan\beta = 1.5$ and $m_0 = 500$ GeV for slices of constant value of M_2. Limits are shown separately for $\mu < 0$ (solid lines) and $\mu > 0$ (dashed lines). Curves for larger values of $\tan\beta$ are in general between those shown for $\mu < 0$ and $\mu > 0$. The corresponding values of mass difference ΔM_+ between the chargino and the lightest neutralino are also shown on scales below the plots.

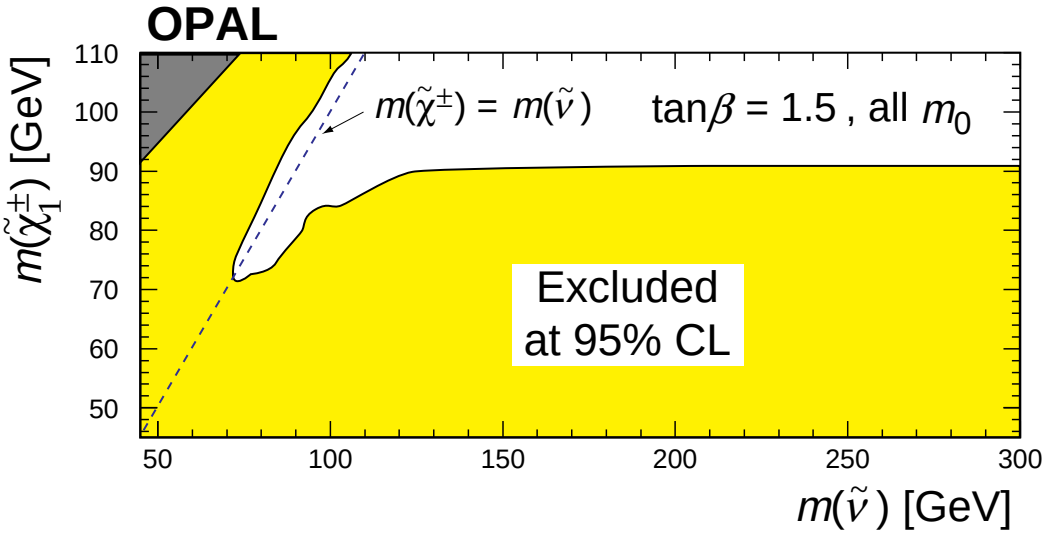

Figure 16: The 95% C.L. excluded region in the ($m_{\tilde{\nu}}$, $m_{\tilde{\chi}_1^+}$) plane for $\tan\beta = 1.5$ and for all m_0 values. The region close to the line of $m_{\tilde{\nu}} = m_{\tilde{\chi}^+}$ where the $\tilde{\chi}_1^+\tilde{\chi}_1^-$ search fails due to small visible energy is excluded using the limits for sneutrinos and OPAL limits for sleptons. The dark shaded region is theoretically inaccessible.

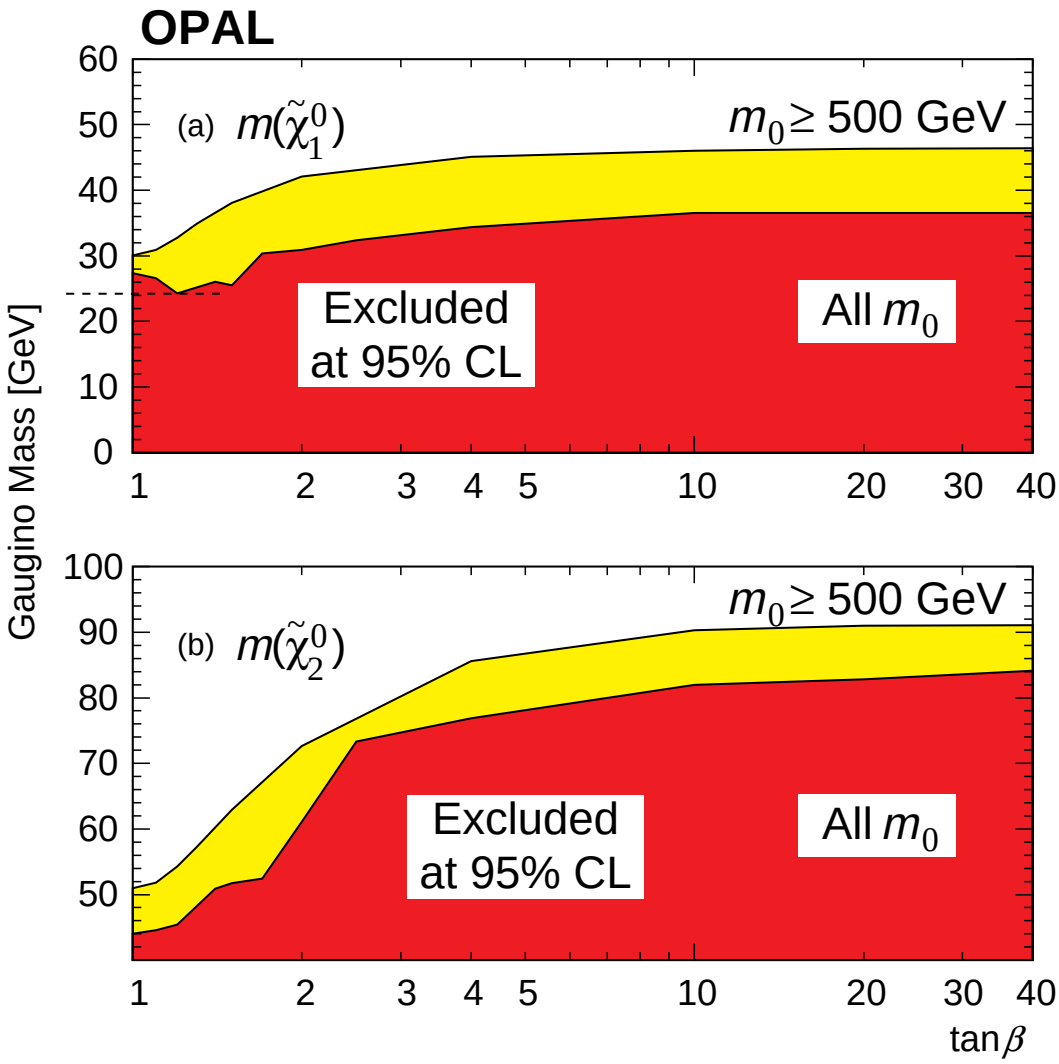

Figure 17: The 95% C.L. mass limit on (a) the lightest neutralino $\tilde{\chi}_1^0$ and (b) the second-lightest neutralino $\tilde{\chi}_2^0$ as a function of $\tan\beta$ for $m_0 \geq 500$ GeV. The mass limit on $\tilde{\chi}_2^0$ is for the additional requirement of $\Delta M_0 > 10$ GeV. The exclusion region for $m_0 \geq 500$ GeV is shown by the light shaded area and the excluded region valid for all m_0 values by the dark shaded area.